



# Effect of Heterogeneous Densification due to Vibroflotation on Liquefaction Resistance

Master of Science Thesis  
ISSN 1652-599X 17:01

Author:  
Alexander Vranckx

Supervisors:  
Stefan Larsson (Kungliga Tekniska Högskolan)  
Patrick Mengé (DEME n.v.)

SCHOOL OF ARCHITECTURE AND BUILT ENVIRONMENT  
May 31, 2017, Stockholm

## Summary

In this thesis the behaviour of a hydraulic fill soil mass containing only fine sand during seismic loading was investigated. More specifically, the effect of vibroflotation was looked at. It is generally accepted that compaction by vibroflotation has a positive effect on the liquefaction resistance. But up till now no generally accepted quantification method exists to assess liquefaction hazard. This can result in discussion between contractors and clients, economic loss and/or an unacceptable liquefaction hazard. Therefore it was investigated whether or not the conservative approach of liquefaction assessment based on the worst CPT after compaction is too conservative, and whether or not horizontal averaging of best and worst CPT is good practice.

After collecting some theoretical knowledge and background information about liquefaction and vibroflotation, a numerical model was constructed in PLAXIS 2D using the HSsmall soil model. The parameters were obtained by correlations with the relative density, for which certain values were assumed, and by means of virtual CPT's which were obtained by back calculating cone tip resistance and sleeve friction correlations with relative density and specific weight, respectively. A grain size distribution was chosen in such a way that the soil was prone to liquefaction and suited to be compacted by vibroflotation.

Volumetric strains indicate whether the soil behaves contractant or dilatant. They thus give an indication on whether liquefaction can occur or not. Therefore the numerical model was used to compare volumetric strains in the uncompacted, compacted and averaged soils. Because volumetric strains in itself can not tell whether liquefaction actually occurs or not, a liquefaction assessment based on an empirical method was carried out in parallel. This way two independent methods were used to assess liquefaction.

The two methods could not really be compared since they investigated different things. But when looking at the uncompacted and the compacted model results it could be seen that they did complement each other reasonably well. This must however be nuanced because the models in which the averaged behaviour was simulated showed somewhat contradictory results when comparing numerical model versus empirical method. The disability of PLAXIS to simulate the liquefaction phenomenon itself was given as a possible explanation for these contradictions.

In most cases a good approximation of the minimum factor of safety against liquefaction in the compacted model was obtained by the average model. Therefore the conclusion was that using the worst CPT as a representation for the whole reclamation site is too conservative regarding liquefaction assessment. However, because of some contradictions in the results and because in some cases the factor of safety got overestimated by the average model, further research was advised on the averaging of best and worst CPT.

# Sammanfattning

I detta examensarbete undersöks det seismiska beteendet av en utfyllnad bestående av finsand och inverkan av vibroflotation. Det är allmänt accepterat att packning med vibroflotation har en positiv effekt på motståndet mot liquefaction men det finns inga allmänt accepterade kvantifieringsmetoder för att bedöma risken för liquefaction. Detta kan resultera i oenighet mellan beställare och entreprenörer, ekonomiska förluster eller en oacceptabel risk för liquefaction. Det har därför studerats om metodiken med riskbedömning baserad på den sämsta CPT-sonderingen är för konservativ och om bedömning baserad på ett genomsnitt av resultaten från den bästa och den sämsta CPT-sonderingen är god praxis.

Efter en genomgång av teori och bakgrundsinformation om liquefaction och vibroflotation upprättades en numerisk modell i PLAXIS 2D med jordmodellen HSmall. Jordparametrarna erhöles från korrelationer med antagna värden av den relativa densiteten och med hjälp av virtuell CPT genom bakåträkning av spetsmotståndets och mantelfriktionens korrelationer med den relativa densiteten respektive den specifika vikten. En kornstorleksfördelning valdes så att liquefaction var benäget att uppstå i jordmaterialet och att det var lämpligt att packa med vibroflotation.

Volymtöjning är mått på om jorden uppvisar kontraktant eller dilatant beteende och indikerar därför om liquefaction kan uppstå eller inte. Den numeriska modellen användes därför till att jämföra volymtöjningar i den opackade, den packade och den genomsnittliga jorden. Eftersom enbart volymtöjningar inte kan avgöra om liquefaction uppstår eller inte gjordes en parallell bedömning baserad på en empirisk metod. På så sätt användes två oberoende metoder för att bedöma potentialen för liquefaction.

De två metoderna kunde inte jämföras direkt eftersom de undersöker olika saker men genom att studera resultaten från den opackade och packade modellen kunde det observeras att de kompletterar varandra relativt väl. Dock visade de numeriska och empiriska metoderna något motsägelsefulla resultat i modellen baserad på genomsnittliga värden. En möjlig förklaring till detta kan vara att PLAXIS inte kan simulera fenomenet med liquefaction.

En god approximation av den lägsta säkerhetsfaktorn mot liquefaction erhöles i den genomsnittliga modellen. Slutsatsen är därför att en bedömning baserad på den sämsta CPT-sonderingen som representation för hela det uppfyllda området är för konservativ. På grund av vissa motsägelsefulla resultat samt att säkerhetsfaktorn i vissa fall överskattades av den genomsnittliga modellen rekommenderas dock fortsatt forskning på bedömningar gjorda med genomsnittliga värden från de bästa och sämsta CPT-sonderingarna.

# Contents

|          |  |           |
|----------|--|-----------|
| <b>1</b> | <b>Introduction</b>                              | <b>1</b>  |
| <b>2</b> | <b>Liquefaction</b>                              | <b>3</b>  |
| 2.1      | Mechanism . . . . .                              | 3         |
| 2.2      | Failure modes . . . . .                          | 3         |
| 2.3      | Liquefaction mitigation . . . . .                | 4         |
| <b>3</b> | <b>Vibroflotation</b>                            | <b>4</b>  |
| 3.1      | Process . . . . .                                | 4         |
| 3.2      | Applicability . . . . .                          | 6         |
| 3.3      | Compaction control . . . . .                     | 6         |
| <b>4</b> | <b>Simulations</b>                               | <b>6</b>  |
| <b>5</b> | <b>Construction of a numerical model</b>         | <b>7</b>  |
| 5.1      | Geometry . . . . .                               | 7         |
| 5.2      | Cone penetrometer test . . . . .                 | 8         |
| 5.3      | Soil model . . . . .                             | 11        |
| 5.3.1    | Unit weight . . . . .                            | 12        |
| 5.3.2    | Void ratio . . . . .                             | 12        |
| 5.3.3    | Damping . . . . .                                | 13        |
| 5.3.4    | Stiffness . . . . .                              | 15        |
| 5.3.5    | Strength . . . . .                               | 16        |
| 5.4      | Earthquake loading . . . . .                     | 16        |
| 5.5      | Boundary conditions . . . . .                    | 16        |
| 5.6      | Mesh and staged construction . . . . .           | 18        |
| <b>6</b> | <b>Liquefaction assessment</b>                   | <b>19</b> |
| 6.1      | Cyclic stress ratio . . . . .                    | 19        |
| 6.2      | Cyclic resistance ratio . . . . .                | 20        |
| <b>7</b> | <b>Results</b>                                   | <b>21</b> |
| 7.1      | CPT results . . . . .                            | 21        |
| 7.2      | Soil parameters . . . . .                        | 23        |
| 7.2.1    | Grain size distribution and void ratio . . . . . | 25        |
| 7.2.2    | Damping . . . . .                                | 26        |
| 7.2.3    | Stiffness . . . . .                              | 27        |
| 7.3      | Simulation results . . . . .                     | 28        |
| 7.4      | Liquefaction assessment . . . . .                | 38        |

|  |           |
|--|-----------|
| <b>8 Discussion</b>  | <b>45</b> |
| 8.1 Simulation results . . . . .   | 45        |
| 8.1.1 Initial stresses . . . . .   | 45        |
| 8.1.2 Volumetric strain . . . . .  | 45        |
| 8.2 NCEER method . . . . .   | 46        |
| 8.3 PLAXIS versus NCEER . . . . .  | 47        |
| <b>9 General conclusion</b>  | <b>48</b> |
| <b>10 Recommended research</b>   | <b>48</b> |
| <b>Appendices</b>  | <b>49</b> |
| A Determination of the dominant frequency in the earthquake input motion . | 49        |
| <b>Acknowledgements</b>  | <b>50</b> |
| <b>References</b>  | <b>50</b> |

## List of Figures

|      |   |    |
|------|---|----|
| 3.1  | Vibroflotation . . . . .  | 5  |
| 5.1  | Grid layout and definition of the model geometry . . . . .                                    | 7  |
| 5.2  | Variation of the relative density over the model width . . . . .                              | 8  |
| 5.3  | $\sigma'_v$ , $\sigma'_p$ and $OCR$ as a function of depth . . . . .                          | 10 |
| 5.4  | Grain size distribution of the sand . . . . .   | 13 |
| 5.5  | Minimum and maximum void ratio as a function of $C_u$ and $R$ , from [18] . . . . .           | 14 |
| 5.6  | Earthquake data . . . . .   | 17 |
| 5.7  | Meshed model . . . . .  | 18 |
| 7.1  | Simulated CPT data . . . . .  | 21 |
| 7.2  | Normalised CPT data . . . . .   | 22 |
| 7.3  | CPT based soil behaviour type chart [25] . . . . .  | 22 |
| 7.4  | Shear wave velocity . . . . .   | 26 |
| 7.5  | Rayleigh damping as a function of frequency . . . . .   | 27 |
| 7.6  | Small strain shear modulus as a function of relative density ( $p_{ref} = 100$ kPa) . . . . . | 27 |
| 7.7  | Initial stress state in the uncompacted model . . . . .                                       | 28 |
| 7.8  | Initial stress states for 4 m probe spacing . . . . .   | 29 |
| 7.9  | Initial stress states for 3.11 m probe spacing . . . . .                                      | 30 |
| 7.10 | Initial stress states for 2.22 m probe spacing . . . . .                                      | 31 |
| 7.11 | Volumetric strains for a probe spacing equal to 4 m, magnitude 6.5 . . . . .                  | 32 |
| 7.12 | Volumetric strains for a probe spacing equal to 4 m, magnitude 7.5 . . . . .                  | 33 |
| 7.13 | Volumetric strains for a probe spacing equal to 3.11 m, magnitude 6.5 . . . . .               | 34 |
| 7.14 | Volumetric strains for a probe spacing equal to 3.11 m, magnitude 7.5 . . . . .               | 35 |
| 7.15 | Volumetric strains for a probe spacing equal to 2.22 m, magnitude 6.5 . . . . .               | 36 |
| 7.16 | Volumetric strains for a probe spacing equal to 2.22 m, magnitude 7.5 . . . . .               | 37 |
| 7.17 | Absolute maximum horizontal surface accelerations . . . . .                                   | 38 |
| 7.18 | $CRR$ , $CSR$ and $FS$ for 4 m probe spacing and $M_w = 6.5$ . . . . .                        | 39 |
| 7.19 | $CRR$ , $CSR$ and $FS$ for 4 m probe spacing and $M_w = 7.5$ . . . . .                        | 40 |
| 7.20 | $CRR$ , $CSR$ and $FS$ for 3.11 m probe spacing and $M_w = 6.5$ . . . . .                     | 41 |
| 7.21 | $CRR$ , $CSR$ and $FS$ for 3.11 m probe spacing and $M_w = 7.5$ . . . . .                     | 42 |
| 7.22 | $CRR$ , $CSR$ and $FS$ for 2.22 m probe spacing and $M_w = 6.5$ . . . . .                     | 43 |
| 7.23 | $CRR$ , $CSR$ and $FS$ for 2.22 m probe spacing and $M_w = 7.5$ . . . . .                     | 44 |

## List of Tables

|     |  |    |
|-----|--|----|
| 5.1 | Model width as a function of grid spacing . . . . .              | 7  |
| 7.1 | Soil parameters . . . . .  | 24 |
| 7.2 | Grain size distribution . . . . .                                | 25 |
| 7.3 | Soil rating based on the suitability number [10] . . . . .       | 25 |
| 7.4 | First eigenfrequency and Rayleigh damping coefficients . . . . . | 26 |
| 7.5 | ‘Best’ CPT location and model center . . . . .                   | 32 |

# List of Symbols

## Latin Symbols

|                           |  |
|---------------------------|--|
| $A_D$ . . . . .           | Constant to determine $G_0^{ref}$  |
| $a_D$ . . . . .           | Constant to determine $G_0^{ref}$  |
| $a_{max}$ . . . . .       | Absolute maximum horizontal surface acceleration   |
| $\mathbf{C}$ . . . . .    | Damping matrix   |
| $c'$ . . . . .            | Effective cohesion   |
| $CRR$ . . . . .           | Cyclic resistance ratio, measure of seismic load resistance                                |
| $CSR$ . . . . .           | Cyclic stress ratio, measure of seismic load   |
| $C_u$ . . . . .           | Coefficient of uniformity, $D_{60}/D_{10}$   |
| $D_{10}$ . . . . .        | Effective diameter, grain size at 10% passage by weight                                    |
| $D_{20}$ . . . . .        | Grain size at 20% passage by weight  |
| $D_{50}$ . . . . .        | Grain size at 50% passage by weight  |
| $D_{60}$ . . . . .        | Grain size at 60% passage by weight  |
| $e$ . . . . .             | Void ratio   |
| $e_{init}$ . . . . .      | Initial void ratio   |
| $e_{max}$ . . . . .       | Maximum void ratio   |
| $e_{min}$ . . . . .       | Minimum void ratio   |
| $E_{oed}^{ref}$ . . . . . | Tangent stiffness for primary oedometer loading  |
| $E_{ur}^{ref}$ . . . . .  | Unloading/reloading stiffness at engineering strains ( $\epsilon = 10^{-3}$ to $10^{-2}$ ) |
| $E_{50}^{ref}$ . . . . .  | Secant stiffness in standard drained triaxial test   |
| $f$ . . . . .             | Frequency [Hz]   |
| $F_r$ . . . . .           | Normalised sleeve friction [%]   |
| $f_s$ . . . . .           | Sleeve friction  |
| $FS$ . . . . .            | Factor of safety against liquefaction  |
| $f_s^{nc}$ . . . . .      | Sleeve friction in normally consolidated soil  |
| $f_s^{oc}$ . . . . .      | Sleeve friction in overconsolidated soil   |
| $g$ . . . . .             | Acceleration due to gravity ( $9.81 \text{ m/s}^2$ )                                       |
| $G_0^{ref}$ . . . . .     | Reference shear modulus at very small strains ( $\epsilon < 10^{-6}$ )                     |
| $H$ . . . . .             | Soil layer thickness [m]   |
| $I_c$ . . . . .           | Soil behaviour type index  |
| $\mathbf{K}$ . . . . .    | Stiffness matrix   |
| $K_c$ . . . . .           | Correction factor for grain characteristics  |
| $K_0^{nc}$ . . . . .      | Coefficient for earth pressure at rest in normally consolidated soil                       |
| $K_0^{oc}$ . . . . .      | Coefficient for earth pressure at rest in overconsolidated soil                            |
| $\mathbf{M}$ . . . . .    | Mass matrix  |
| $m$ . . . . .             | Power for stress-level dependency of stiffness   |
| $MSF$ . . . . .           | Magnitude scaling factor   |
| $M_w$ . . . . .           | Moment magnitude   |
| $n$ . . . . .             | Soil dependent exponent  |

|                            |  |
|----------------------------|--|
| $n_D$ . . . . .            | Constant to determine $G_0^{ref}$  |
| $OCR$ . . . . .            | Overconsolidation ratio, ratio of current effective vertical stress and highest effective vertical stress of the soil's stress history |
| $p$ . . . . .              | Pressure   |
| $p_a$ . . . . .            | Atmospheric pressure (100 kPa)   |
| $p_{ref}$ . . . . .        | Reference pressure (100 kPa)   |
| $q_c$ . . . . .            | Uncorrected cone tip resistance  |
| $q_c^{oc}$ . . . . .       | Uncorrected cone tip resistance in overconsolidated soil   |
| $q_{c1N}$ . . . . .        | Normalised tip resistance for liquefaction assessment  |
| $(q_{c1N})_{cs}$ . . . . . | Equivalent clean-sand normalised tip resistance for liquefaction assessment  |
| $Q_{tn}$ . . . . .         | Normalised tip resistance  |
| $Q_{tn}^{nc}$ . . . . .    | Equivalent normally consolidated normalised tip resistance   |
| $q_t$ . . . . .            | Corrected cone tip resistance for pore water effects   |
| $R$ . . . . .              | Roundness of grains  |
| $r_d$ . . . . .            | Stress reduction coefficient   |
| $R_e$ . . . . .            | Relative density [%]   |
| $R_f$ . . . . .            | Failure ratio of the hyperbolic constitutive model   |
| $V_s$ . . . . .            | Shear wave velocity [m/s]  |
| $x_{CPT}$ . . . . .        | $x$ -coordinate of CPT measurement at 1/3 of grid spacing distance   |
| $x_{middle}$ . . . . .     | $x$ -coordinate at the middle of the model   |
| $z$ . . . . .              | Depth [m]  |

## Greek Symbols

|                               |  |
|-------------------------------|--|
| $\alpha$ . . . . .            | Rayleigh damping constant indicating portion of the mass matrix      |
| $\beta$ . . . . .             | Rayleigh damping constant indicating portion of the stiffness matrix |
| $\gamma_{sat}$ . . . . .      | Saturated unit weight of soil  |
| $\gamma_{unsat}$ . . . . .    | Unsaturated unit weight of soil                                      |
| $\gamma_w$ . . . . .          | Unit weight of water (9.81 kN/m <sup>3</sup> )                       |
| $\gamma_{0.7}$ . . . . .      | Shear strain at which $G_s = 0.722G_0$                               |
| $\Delta n$ . . . . .          | Difference between current and previous value of $n$                 |
| $\epsilon_v$ . . . . .        | Volumetric strain  |
| $\nu_{ur}$ . . . . .          | Poisson's ratio for unloading/reloading                              |
| $\xi$ . . . . .               | Damping ratio  |
| $\sigma'_p$ . . . . .         | Effective preconsolidation pressure                                  |
| $\sigma_t$ . . . . .          | Tensile strength   |
| $\sigma_v$ . . . . .          | Total vertical stress  |
| $\sigma_v^{eff}$ . . . . .    | Effective vertical stress  |
| $\sigma'_v$ . . . . .         | Effective vertical stress  |
| $\sigma_{xx}^{eff}$ . . . . . | Effective horizontal stress  |
| $\tau_{av}$ . . . . .         | Average cyclic shear stress  |
| $\phi'$ . . . . .             | Effective peak friction angle  |

|                        |   |
|------------------------|---|
| $\phi'_{nc}$ . . . . . | Effective peak friction angle in normally consolidated soil |
| $\phi'_{oc}$ . . . . . | Effective peak friction angle in overconsolidated soil      |
| $\psi$ . . . . .       | Dilatancy angle   |
| $\omega$ . . . . .     | Angular frequency [rad/s]                                   |

# 1 Introduction

Because hydraulic fills consist of loose saturated sands, they are prone to liquefaction due to earthquakes. Liquefaction (section 2) is a phenomenon caused by the loss of shear strength of saturated cohesionless soil due to for example seismic loading. Because of the undrained character of this type of loading, the pore water has no time to be expelled out of the soil and excess pore pressures arise. Due to these excess pore pressures, effective stresses in the soil decrease and a subsequent loss of shear strength is obtained. In the extreme case that effective stresses become zero, soil particles are not longer in contact with each other and the soil behaves like a fluid, hence the name ‘liquefaction’.

To prevent liquefaction, liquefaction mitigating measures need to be taken. One possible way to do this is by compacting the hydraulic fill. Due to compaction the tendency of loose soil to contract upon shearing will decrease, or the soil will even behave dilatant. This way the build up of excess pore pressures is limited or prevented and liquefaction is less likely to occur.

Vibroflotation (section 3) is a deep vibratory compaction technique that is able to compact a complete soil column (except for the top layer which needs additional compaction by means of for example compaction rollers). The method uses a specific vibrating probe that is inserted into the soil until the required depth is reached. By means of strong horizontal vibrations and full saturation obtained by water jetting at the side of the vibrator, a state of local liquefaction is obtained. This way the particles are temporarily free to move and able to settle into a denser state. The probe is pulled back to the surface in multiple steps, and doing so the complete soil column gets compacted. To cover the complete site, the method is applied in a grid (triangular or square). This thesis focussed on the use of a triangular grid because of its higher efficiency compared to a square grid.

Inherent to the method, and typical for working in a grid configuration, is that the site is compacted heterogeneously. This might lead to problems concerning differential settlements causing damage to overlying structures. This problem can however be solved by compacting the top layer of the soil by compaction rollers to obtain a more homogeneous top layer.

Liquefaction assessment is usually based on the worst result (i.e. lowest cone tip resistance) of a Cone Penetration Test (CPT) obtained over (a part of) the site. Normally, it is located at the centroid of the triangle formed by 3 penetration points. Using this measurement as a representative for the whole site is considered conservative and therefore safe. However, because the more compacted zones might take some of the load and can possibly support liquefied soil in between them, this conservative approach might be too conservative and therefore uneconomic. A horizontal averaging of ‘best’ and worst CPT result is suggested by contractors to obtain a more realistic liquefaction assessment. This average approach is generally accepted regarding bearing capacity and required density, but it is generally not allowed when looking at liquefaction because of the risk of underestimating the liquefaction hazard.

A numerical model (sections 4 and 5) in the commercial software PLAXIS 2D was used to investigate the liquefaction mitigating effects of vibroflotation and to check whether or

not horizontal averaging is good practice. The Hardening Soil Small strain stiffness model (HSsmall) was used to simulate the soil behaviour. The parameters necessary for its implementation were obtained via correlations with the relative density and by means of virtual CPT's created by back calculating cone tip resistance and sleeve friction correlations with relative density and specific weight, respectively. Earthquakes with moment magnitude 6.5 and 7.5 were simulated and three different grid spacings were used.

Two approaches were followed. First the volumetric strains in the soil mass were investigated in multiple points because they indicate contraction or dilation. The results are shown as a function of time during the earthquake in section 7.3. Second, an empirical method was used in combination with simulated surface accelerations to do a liquefaction assessment to determine whether liquefaction actually occurs or not (section 6). The results are shown as contour plots of the seismic resistance, seismic load and the factor of safety against liquefaction over the complete simulated soil body in section 7.4.

Section 8 discusses and compares the results of the two approaches, and a conclusion with respect to whether or not the current method of liquefaction assessment is too conservative, and that horizontal averaging is good practice or not, is made in section 9. Finally, section 10 gives recommendations for continuation of the research done in this thesis.

## 2 Liquefaction

Liquefaction is an important cause of damage during earthquakes. But it wasn't until the earthquakes in Niigata, Japan [1], and Anchorage, Alaska [2] in 1964 that research really developed. Different types of damage can occur due to liquefaction, a.o. subsidence and tilting of structures [3]. Especially hydraulic fills are prone to liquefaction because they consist of loose saturated sand.

### 2.1 Mechanism

Phenomena that have to do with soil deformations caused by monotonic, transient or repeated disturbance of saturated cohesionless soils under undrained conditions can generally be captured under the term liquefaction [4]. The undrained character of rapid dynamic loading in combination with the tendency of loose sandy soils to contract (i.e. decrease of pore volume) during shearing gives rise to an increase in pore pressure with time [5][6].

According to following relation which defines effective stress, effective stresses will decrease when pore pressures increase [7]:

$$\text{Effective stress} = \text{Total stress} - \text{Pore pressure}$$

Effective stresses represent contact forces between grains. This means that contact force between the grains decreases with increasing pore pressure. In the extreme case, i.e. when effective stresses become zero, there is no contact between the grains, and the particles are suspended in the pore water. The soil then behaves as a dense fluid (mud) and hence the term 'liquefaction'. [8]

### 2.2 Failure modes

The failure behaviour of liquefied soil can be divided into two types: flow liquefaction and cyclic mobility. Flow liquefaction can occur when the shear strength of the soil no longer suffices to keep static equilibrium of a soil mass. Cyclic stresses may cause the strength of the soil to drop so that an unstable state is reached in which static shear stresses can cause flow failure. Flow liquefaction gives rise to large deformations which are driven by static shear stresses.

Cyclic mobility, in contrast to flow liquefaction, occurs when the shear strength of the liquefied soil is higher than the static shear stresses. Cyclic mobility gives rise to incrementally increasing deformations during earthquake shaking, driven by both cyclic and static shear stresses. [4][9] In what follows these two types of behaviour are captured under the name 'liquefaction failure'.

On horizontal ground in which all the existing stresses are only caused by the self-weight of the soil, three liquefaction failure mechanisms can be distinguished [9]:

- sand boils
- subsidence and settlement

- differential transient motions

Sand boils refer to an upward flow of water caused by excess pore pressures at a certain depth. If the gradient of this flow is large enough, the flow will drag the soil particles with it to the surface through cracks or thinner spots in the upper stratum (in perfectly homogeneous soils a state of quicksand would arise over the whole liquefied site).

Subsidence and settlements occur with the dissipation of the excess pore pressures. When these settlements are uneven, or when unacceptable values regarding serviceability are reached, damage will occur.

Differential transient motions might occur during earthquake shaking because of the lower stiffness of liquefied soils. This means that the top of the soil layer can move relative to the bottom of the soil layer. This can lead to damage of underground structures like pile foundations, tunnels or pipelines.

## 2.3 Liquefaction mitigation

A broad array of liquefaction mitigation measures is available to prevent liquefaction or to limit the detrimental effects. Based on parameters like feasibility, secondary effects and economics, a choice can be made [9]. A number of liquefaction mitigation methods are summarised below:

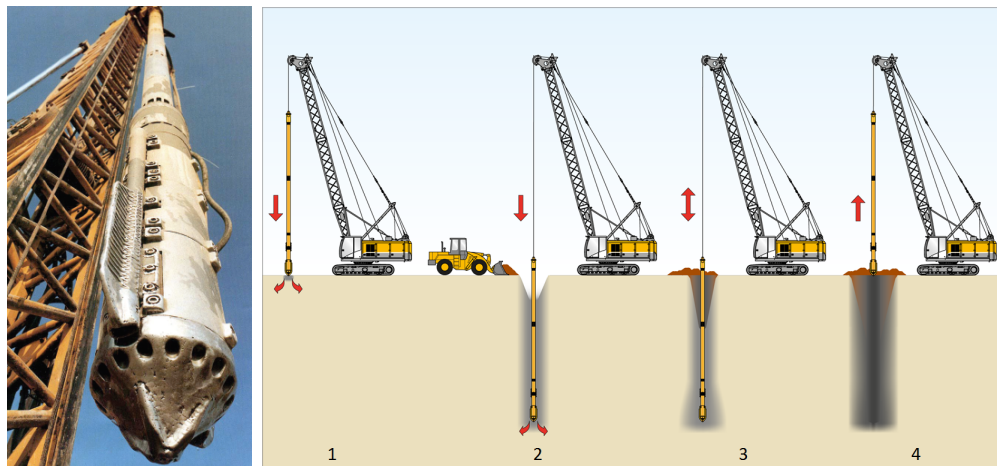
- Vibroflotation [10]
- Vibro wing method [11]
- Vibro-replacement (stone columns) [12][13]
- Deep soil mixing [14][15]
- (Columnar gravel) Drains [16]

## 3 Vibroflotation

Vibroflotation is a deep vibratory compaction method that is used in non-cohesive soils up to depths of 40 to 50 meters. It was introduced for the first time in Germany in 1934 [17]. Its principle is to rearrange the soil particles in a denser packing by means of horizontal vibrations caused by a specially designed probe, called a vibroflot (figure 3.1a).

### 3.1 Process

The vibroflot, extended with the necessary extension tubes to reach the required depth, is suspended on a crane (1 in figure 3.1b). It is then lowered onto the ground and by means of vibrations and its own weight, whether or not aided by water or air jetting at the tip, the vibroflot penetrates until the desired depth (2 in figure 3.1b). After reaching the required

(a) Vibroflot,  
from [18]

(b) Vibroflotation process, after [19]

Figure 3.1: Vibroflotation

depth, the vibroflot is pulled back up stepwise, allowing for the soil to compact in each step (3 in figure 3.1b). When the vibroflot reaches the ground surface again, a heterogeneous compacted soil column is established in which the soil is less compacted further away from the penetration point (4 in figure 3.1b) [17].

To compensate for the loss in volume due to compaction, extra material is added at the tip of the vibrating probe. This can be done by adding the material in the annulus around the vibrator at the ground surface by means of for instance a wheel loader (2 and 3 in figure 3.1b). This method is called the top feed method. While adding the material, lateral water jets installed on the vibroflot are enabled. This way an upward waterflow is realised which prevents the annulus around the vibrator from collapsing and allows the added material to reach the tip of the vibrator [10].

Another method, the bottom feed method, requires a different type of vibrator. This vibrator is equipped with a pipe, running from a reservoir at the top to the tip of the vibrator. The material is added into the reservoir and exits the pipe at the tip of the vibrator to compensate the volume loss due to compaction. [20] The following focuses only on the use of the top feed method.

The vibrating motion of the vibroflot is caused by excentric masses rotating in a horizontal plane driven by electric or hydraulic engines. The degree of compaction in each step is monitored by means of the power needed by the engine to rotate the excentrics at a constant frequency. The more compacted, the more power is needed. For hydraulically driven vibrators, the oil pressure indicates the degree of compaction in the same way. [10]

Due to the lateral water jets, also used to prevent the annulus around the vibrator from collapsing, a full degree of saturation is reached in the surroundings of the vibroflot. Combined with the strong vibratory motion induced by the vibroflot, a local state of liquefaction is reached. This allows the particles to settle into a denser state. [18]

### 3.2 Applicability

Only granular materials are suited for this compaction technique since an increase in fines content will decrease the permeability of the soil and hence the efficiency. In general, the maximum fines content is restricted to 15%. [21] Above this, other compaction methods like the vibro replacement stone column technique are recommended [17].

### 3.3 Compaction control

Control of the compacted site is first of all done by recording parameters like the required power or oil pressure, water flow, vibration time per pull back step and so on during the compaction process. Also after compaction controls are performed. Commonly this is done by means of standard penetration tests (SPT) or cone penetration tests (CPT). The latter is preferred because of its ability to produce a continuous profile throughout the soil column and because of its high productivity. [22]

Compaction criteria are often formulated in terms of relative density, cone tip resistance (CPT), stiffness or settlements [23]. Because relative density was used as a main parameter in this thesis, correlations between relative density and CPT's were used.

## 4 Simulations

Three different types of simulations were performed. The first type, the uncompacted model, consisted of only uncompacted soil. The second type, the compacted model, simulated the compacted soil and contained thus the range of soils from most compacted to least compacted (figure 5.2). The third and last type, the average model, consisted of only the soil represented by the average of the cone tip resistance and sleeve friction of the least compacted soil and the soil at 1/3 of the compaction point spacing from the best compacted point (CPT point closest to a compaction point in figure 5.1). This distance was chosen because contractors generally perform a CPT at this place to obtain a 'best' CPT result regarding required density and bearing capacity. These three model types were simulated with both magnitude 6.5 earthquake loading and magnitude 7.5 earthquake loading, resulting in a subtotal of 6 simulations.

The probe spacing is a very important parameter for the production of the vibroflotation method. Therefore the three simulation types mentioned above were carried out for different probe spacings: 4 m, 3.11 m and 2.22 m. The probe spacing of 4 m was chosen as an upper boundary based research performed by Brown [10] and on personal communication with the supervisor. The probe spacings of 3.11 m and 2.22 m were chosen in such a way that a realistic range of grid spacings was covered, and that in the numerical model the same zone widths (see further, section 5.1) could be kept. Combined with the three types of simulations and the two earthquake magnitudes, this resulted in 18 simulations in total.

## 5 Construction of a numerical model

### 5.1 Geometry

To investigate the behaviour of a hydraulic fill soil mass during earthquake shaking, a numerical model was constructed with the commercial software PLAXIS 2D with the Dynamics add-on module. Because the 2D-model used a plain-strain condition, the real ‘3D-situation’ needed to be converted to a plain strain equivalent. This was done by simply unfolding the line ABC to a straight line as shown on figure 5.1. This method was chosen because it captures the best and worst compacted point in the compaction grid and because doing so, a symmetrical model was achieved.

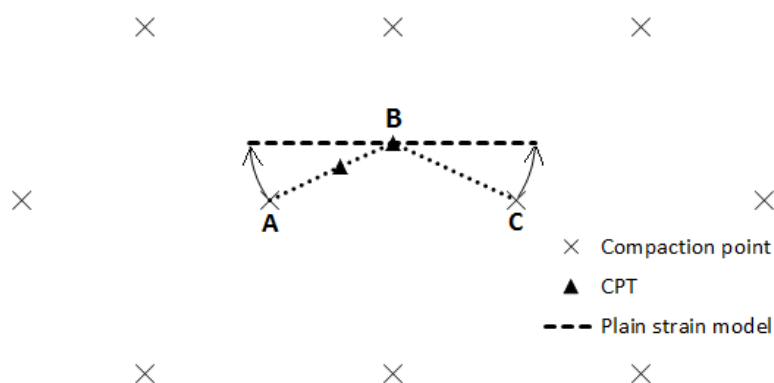


Figure 5.1: Grid layout and definition of the model geometry

The cross section of the model was based on general parameters common in land reclamation projects. A 10 m thick sand layer was considered, overlaying bed rock. The water table was assumed to be at 4 m below the ground surface. Therefore liquefaction could only occur in the bottom 6 m of the model.

The soil column width is dependent on the simulated grid spacing and could be derived simply from the geometry of the grid shown in figure 5.1 (length of the line ABC). Table 5.1 summarises the simulated grid spacings and the corresponding model widths. The width

Table 5.1: Model width as a function of grid spacing

| Grid spacing [m] | Model width [m] |
|------------------|-----------------|
| 4.00             | 4.62            |
| 3.11             | 3.59            |
| 2.22             | 2.57            |

of the model was divided into different zones ranging from top to bottom and 26 cm wide (except for the zones near the edges of the model which were only half the width due to symmetry). This division was made to allow for introducing the varying relative density caused by the vibroflotation process.

The relative density  $R_e$  was assumed to be 70% for the best compacted soil, and 40% for the uncompacted soil [10]. The decrease in relative density away from the compaction point was assumed to be linear<sup>1</sup>, and the decrease rate was equal in all models which means that the influence radius of the vibroflot was taken as a constant (overlap of compacted zones was hereby not considered). Figure 5.2 shows the distribution of the relative density across the line ABC in figure 5.1 for the three simulated grid spacings.

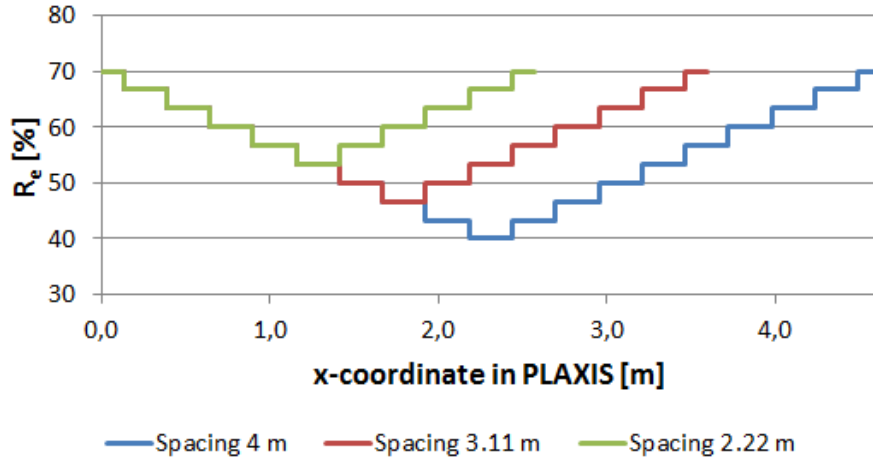


Figure 5.2: Variation of the relative density over the model width

## 5.2 Cone penetrometer test

Because no real measurements were used in this thesis, a virtual CPT was simulated to derive some of the model parameters and to assess the liquefaction risk. The cone tip resistance  $q_c$  and the sleeve friction  $f_s$  were based on the correlations given in equations 5.1 [24] and 5.2 [25]:

$$R_e = \frac{1}{2.91} \ln \left( \frac{q_c}{61\sigma_v^{0.71}} \right) 100\% \quad (5.1)$$

$$\frac{\gamma_{unsat}}{\gamma_w} = 0.27 \log \left( \frac{f_s}{q_c} 100\% \right) + 0.36 \log \left( \frac{q_c}{p_a} \right) + 1.236 \quad (5.2)$$

where  $R_e$  is the relative density,  $\sigma_v'$  is the vertical effective stress,  $\gamma_{unsat}$  the unsaturated unit weight of the soil,  $\gamma_w$  the unit weight of water (9.81 kN/m<sup>3</sup>) and  $p_a$  the atmospheric pressure equal to 100 kPa.

<sup>1</sup>Depending on how long the vibroflot is left vibrating at the same depth before being lifted to the next step, this linear approach might over- or underestimate the achieved density [17]. The linear decrease was chosen as an approximation without conducting further research on the dependency on the vibration time per step.

Because a sandy soil was used no correction of the tip resistance regarding pore pressures had to be made ( $q_t = q_c$ ) [25]. Therefore only  $q_c$  was used further in the elaboration which is based on the CPT Guide by Robertson et al. [25].

Normalising the tip resistance and the sleeve friction with equations 5.3 and 5.4, respectively, yielded the normalised tip resistance  $Q_{tn}$  and the normalised friction ratio  $F_r$  [25]:

$$Q_{tn} = \left( \frac{q_c - \sigma_v}{p_a} \right) C_n \quad \text{with} \quad C_n = \left( \frac{p_a}{\sigma'_v} \right)^n \quad (5.3)$$

$$F_r = \frac{f_s}{q_c - \sigma_v} 100\% \quad (5.4)$$

where  $\sigma_v$  is the total vertical stress.

The exponent  $n$  in equation 5.3 had to be determined iteratively. In the first iteration  $n$  was equal to 1.00 and the soil behaviour type index  $I_c$ , which indicates the soil type (see further, figure 7.3), could be calculated [25]:

$$I_c = [(3.47 - \log Q_{tn})^2 + (\log F_r + 1.22)^2]^{0.5} \quad (5.5)$$

The value of  $I_c$  obtained with equation 5.5 allowed for calculating a new value of  $n$ :

$$n = 0.381I_c + 0.05 \frac{\sigma'_v}{p_a} - 0.15 \leq 1.0 \quad (5.6)$$

$Q_{tn}$  was then recalculated with the new value of  $n$ . This iterative procedure was repeated until  $\Delta n < 0.01$ , with  $\Delta n$  equal to the absolute difference between the current  $n$ -value and the previous  $n$ -value.

The procedure to obtain the normalised tip resistance as given above is only valid for normally consolidated soils because equations 5.1 and 5.2 are only valid for normally consolidated soils. Compaction of the soil will, however, lead to an increase in the horizontal stresses and the overconsolidation ratio of the soil [26]. Therefore, the virtual CPT data that were used above had to be adjusted for this.

Higher horizontal stress will cause the cone tip resistance and the sleeve friction to rise. The increase in cone tip resistance was taken into account based on Salgado et al. [27] where an additional normalization of the cone tip resistance with the horizontal stresses was suggested. The cone tip resistance in overconsolidated soil,  $q_c^{oc}$ , could then be found using the following equation:

$$Q_{tn}^{nc} = C_{nh} C_n \left( \frac{q_c^{oc} - \sigma_v}{p_a} \right) \quad \text{with} \quad C_{nh} = \sqrt{\frac{K_0^{nc}}{K_0^{oc}}} \quad (5.7)$$

where  $Q_{tn}^{nc}$  is the equivalent normally consolidated normalised tip resistance as found with the derivation given above for normally consolidated soil,  $q_c^{oc}$  is the tip resistance corrected for the increased horizontal stresses in overconsolidated soils and  $K_0^{nc}$  and  $K_0^{oc}$  are the earth pressure coefficients at rest for normally consolidated and overconsolidated soil, respectively.

The overconsolidation ratio,  $OCR$ , was assumed to vary linearly from 1 for the uncompacted (normally consolidated) soil (Soil 1) to 5 for the most compacted soil (Soil 10), which corresponds approximately to a doubling of the horizontal stresses [26]. The  $OCR$  was also assumed to be constant over the depth. This is a simplification because the  $OCR$  is a depth-dependent parameter.

In PLAXIS it is possible to take into account the depth-dependency of the  $OCR$  by either dividing the model into horizontal layers and assigning a certain  $OCR$  to each layer, or by using a constant Pre-Overburden Pressure ( $POP$ ) [28]. The first option was not possible because the  $OCR$  profile was not exactly known. The second option, using a constant  $POP$  is perfectly suited for describing the natural situation of horizontally layered soil from which a part has eroded. But it does not necessarily apply to the case of compacted soil when it is compacted by means of horizontal vibrations (which is not a vertical load). Following example clarifies the above:

Assume a homogeneous soil layer with a thickness of 10 m and a specific weight of  $20 \text{ kN/m}^3$ . The water table is assumed to be more than 10 m below the ground surface. The effective vertical stresses can then easily be calculated by multiplying the depth with the specific weight (figure 5.3).

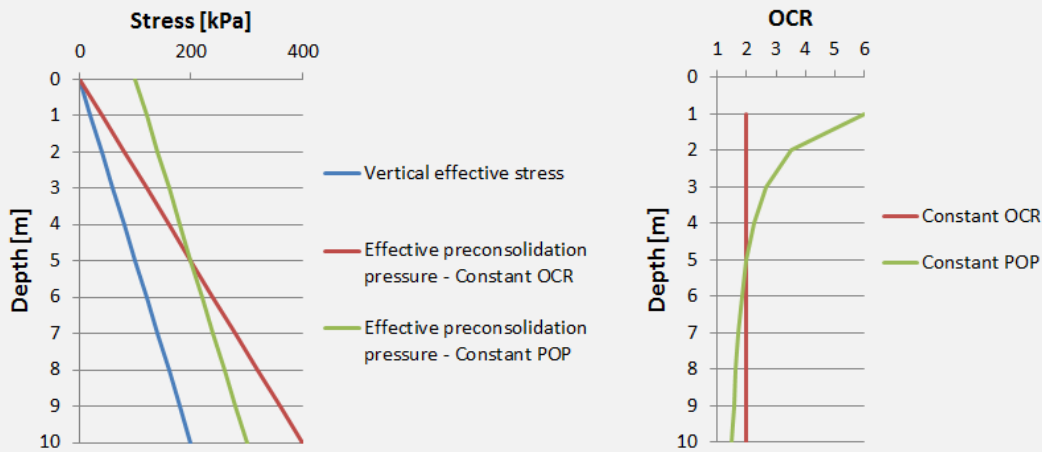


Figure 5.3:  $\sigma'_v$ ,  $\sigma'_p$  and  $OCR$  as a function of depth

Now assume that in the past a 5 m thick soil layer covered the 10 m thick layer (for simplicity the same soil is assumed), but it has eroded now. In this case, the 5 m soil layer has served as a constant  $POP$  equal to 100 kPa. This means that the resulting effective preconsolidation pressure in the 10 m thick layer is 100 kPa higher than the effective stress over the entire depth (figure 5.3). The related  $OCR$ , as shown in figure 5.3, can be calculated as follows:

$$OCR = \frac{\sigma'_p}{\sigma'_v} \quad (5.8)$$

In the case of a constant  $OCR = 2$ ,  $\sigma'_p$  can be calculated by converting equation 5.8. The resulting effective preconsolidation pressure is also shown in figure 5.3.

This example shows that in the case of a constant  $OCR$ ,  $\sigma'_p$  increases faster with depth. This means that the soil will remain in the elastic region over a larger stress range at larger depths (below the crossing of the red and the green line). Applied to the subject of liquefaction, this means that at larger depths large plastic deformations are less likely to occur and that therefore liquefaction is less likely to occur.

The earth pressure coefficients at rest were calculated as the default values in PLAXIS [28]. Equations 5.9 and 5.10 show how the default values in PLAXIS were obtained:

$$K_0^{nc} = 1 - \sin \phi' \quad (5.9)$$

$$K_0^{oc} = K_0^{nc} OCR - \frac{\nu_{ur}}{1 - \nu_{ur}} (OCR - 1) \quad (5.10)$$

where  $\nu_{ur}$  is Poisson's ratio for unloading/reloading.

The increase in sleeve friction from  $f_s^{nc}$  for uncompacted soil to  $f_s^{oc}$  for compacted soil was based on the findings of Massarsch et al. [26] with the assumption that the increase in friction angle  $\phi'$  due to overconsolidation caused by the compaction process is negligible (Equation 5.11). This assumption is conservative because the friction angle is a strength parameter which was underestimated here.

$$\frac{f_s^{oc}}{f_s^{nc}} = \frac{K_0^{oc} \tan \phi'_{oc}}{K_0^{nc} \tan \phi'_{nc}} \quad (5.11)$$

The newly obtained parameters  $q_c^{oc}$  and  $f_s^{oc}$  could then be normalised again by the iterative procedure explained above.

### 5.3 Soil model

To simulate the dynamic behaviour of the soil, the Hardening Soil model with small strain stiffness (HSsmall) in PLAXIS 2D was used. This model takes into account the very small-strain soil stiffness and its non-linear dependency on strain amplitude [29]. Because of this, hysteretic behaviour was obtained for unloading/reloading causing hysteretic strain dependent damping under dynamic loading. The HSsmall model is not able to generate accumulated strains with multiple loading cycles nor does it calculate pore pressures for undrained cases. It is, however, able to simulate contractant and dilatant behaviour, which plays a major role in the liquefaction phenomenon. Contractant behaviour is namely necessary for the generation of excess pore pressures and the corresponding decrease in effective stress causing liquefaction.<sup>2</sup>

<sup>2</sup>The PLAXIS HSsmall model is not able to simulate the liquefaction phenomenon itself. Although more advanced models exist to simulate liquefaction [30][31], it was opted to use a simplified method based on volumetric strain.

### 5.3.1 Unit weight

The unsaturated unit weight  $\gamma_{unsat}$  and the saturated unit weight  $\gamma_{sat}$  were calculated using equations 5.12 and 5.13, respectively. These correlations were published by Brinkgreve et al. [32]. There the correlations were validated against lab test data for different sands at different densities and different pressures.

$$\gamma_{unsat} = 14 + 4.2 \cdot \frac{R_e}{100} \quad [\text{kN/m}^3] \quad (5.12)$$

$$\gamma_{sat} = 19 + 1.6 \cdot \frac{R_e}{100} \quad [\text{kN/m}^3] \quad (5.13)$$

### 5.3.2 Void ratio

Since values for the relative density were assumed (section 5.1), the value of the related initial void ratio  $e_{init}$  could be determined very easily based on the definition of the relative density given in equation 5.14.

$$R_e = \frac{e_{max} - e_{init}}{e_{max} - e_{min}} \quad (5.14)$$

The minimum and maximum void ratio, however, were not known and depend on soil characteristics like the grain size distribution – more specific the coefficient of uniformity  $C_u$  – and the roundness of the grains  $R$  (not to be confused with  $R_e$  which stands for the relative density) [33].

The grain size distribution was chosen freely by the author, taking into account the fact that the soil had to be suitable for the vibroflotation process, and, that the soil was likely to liquefy under earthquake conditions. Figure 5.4 shows the grain size distribution together with the boundaries indicating the suitability for vibroflotation [10] and the limits between which soils are prone to liquefaction [34]. Zone A hereby represents a zone of material that is too coarse for the use of vibroflotation as a means of compaction. Due to the high strength of the material, the penetration of the probe into the soil prior to compaction would go very slow, if not impossible, and therefore the method is uneconomic in zone A. Zone B represents grain sizes for which vibroflotation is a very good method of compaction. Zone C represents the materials that are too fine to achieve high efficiency in the vibroflotation process. It is, however, allowed for part of the grain size distribution to be situated in zone C. Fines content should, however, remain under 10% to 15%.

Because the zone which is prone to liquefaction is almost completely situated in zone C, and because only part of the grain size distribution could be part of zone C in order to be still suited for vibroflotation, careful consideration was made for the choice of the grain size distribution. It was chosen by the author to let the curve be in zone B (and thus outside the ‘prone to liquefaction zone’ but suited for vibroflotation) partly, coincide with the upper boundary of the ‘prone to liquefaction zone’ in zone C (and thus less suited for vibroflotation) for the middle part, and to be in the ‘prone to liquefaction zone’ and in zone B (meaning prone to liquefaction and suited for vibroflotation) for the last part.

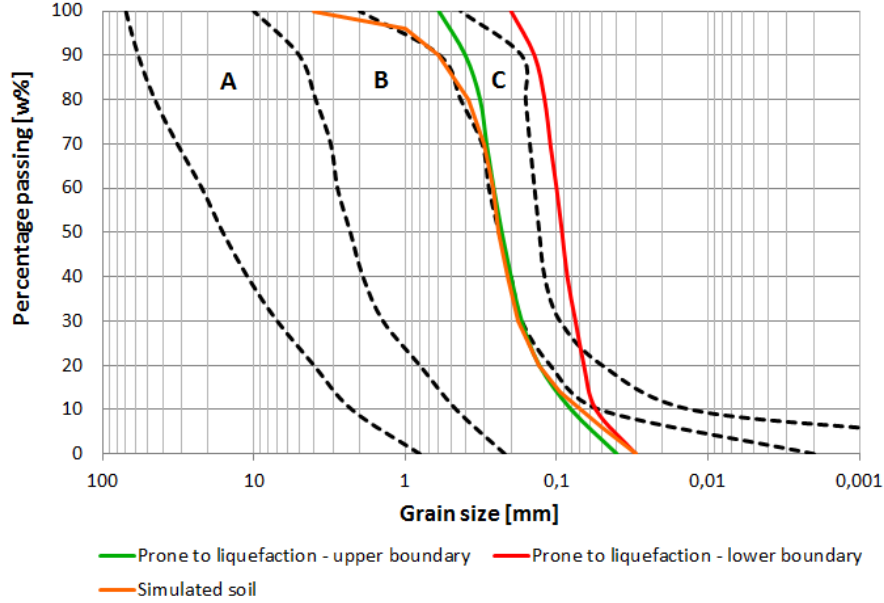


Figure 5.4: Grain size distribution of the sand

From this grain size distribution, the coefficient of uniformity  $C_u$  could easily be calculated as:

$$C_u = \frac{D_{60}}{D_{10}} \quad (5.15)$$

where  $D_{10}$  and  $D_{60}$  are the diameters corresponding to 10% and 60% passage by weight, respectively. Based on the assumption of angular soil particles ( $R = 0.20$ ), the minimum and maximum void ratio can be read from the diagram shown in figure 5.5.

### 5.3.3 Damping

Frequency independent/strain dependent material damping was incorporated in the HS-small model by means of the hysteretic behaviour of the soil model upon cyclic loading [29]. But for low strain amplitudes this type of damping becomes very small because of the nearly linear elastic behaviour of the constitutive model. Therefore viscous damping was introduced in the model by means of Rayleigh damping [35][36].

Rayleigh damping is commonly introduced in numerical models because of its computational ease. When using this type of damping, the damping matrix  $\mathbf{C}$  is constructed with part of the mass matrix  $\mathbf{M}$  and part of the stiffness matrix  $\mathbf{K}$  as shown in equation 5.16. [37]

$$\mathbf{C} = \alpha\mathbf{M} + \beta\mathbf{K} \quad (5.16)$$

The damping constants  $\alpha$  and  $\beta$  were calculated by PLAXIS after providing the target frequencies  $\omega_i = 2\pi f_i$  and  $\omega_j = 2\pi f_j$  and the corresponding target damping ratios  $\xi_i$  and

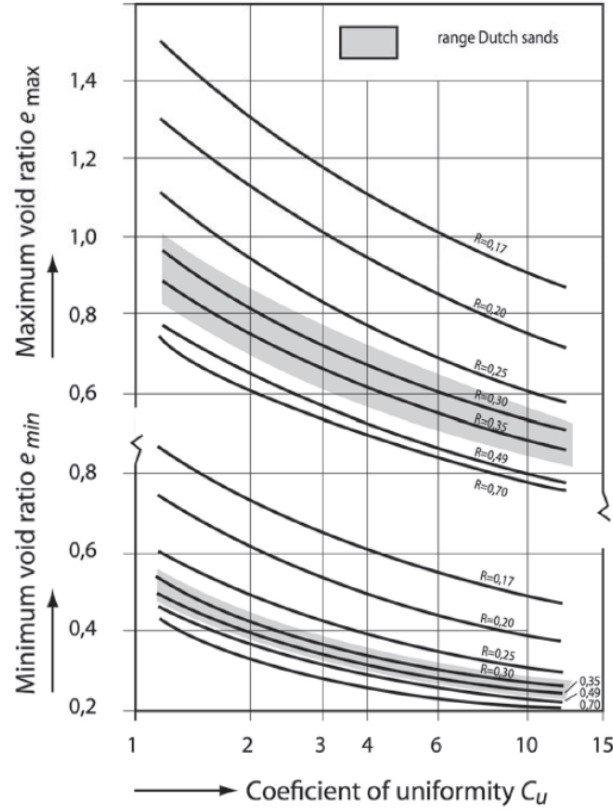


Figure 5.5: Minimum and maximum void ratio as a function of  $C_u$  and  $R$ , from [18]

$\xi_j$  by solving following system of equations:

$$\frac{1}{2} \begin{bmatrix} 1/\omega_i & \omega_i \\ 1/\omega_j & \omega_j \end{bmatrix} \begin{bmatrix} \alpha \\ \beta \end{bmatrix} = \begin{bmatrix} \xi_i \\ \xi_j \end{bmatrix} \quad (5.17)$$

$f_i$  and  $f_j$  were determined using the procedure given in Hudson et al. [38]. There  $f_i$  corresponds to the first eigenfrequency  $f_1$  of the soil column which could be found using following equation:

$$f_1 = \frac{V_{s,avg}}{4H} \quad (5.18)$$

where  $V_{s,avg}$  and  $H$  are the average shear wave velocity over the depth and the soil layer thickness, respectively.

The shear wave velocity profile, of which the average was determined, was derived for each soil from the virtual CPT data calculated in section 5.2 by equation 5.19 [25].

$$V_s = \left[ \alpha_{V_s} \frac{q_c - \sigma_v}{p_a} \right]^{0.5} \quad \text{with} \quad \alpha_{V_s} = 10^{0.55I_c + 1.68} \quad (5.19)$$

The second target frequency  $f_j$  was taken equal to the  $n^{th}$  eigenfrequency  $f_n$  of the soil. Where  $n$  was the closest odd integer larger then the ratio  $f_e/f_1$  with  $f_e$  being the dominant

frequency in the input earthquake accelerations.  $f_e$  was determined by taking the Fourier transformation of the input acceleration time series and then looking with which frequency the highest amplitude corresponds.

### 5.3.4 Stiffness

The HSsmall model requires the input of several stiffness related parameters. Since – as mentioned earlier – no real measurements were used in this thesis, the values of these parameters were based on correlations found in literature. The required stiffness parameters are summarised below [28]:

- $E_{50}^{ref}$ , secant stiffness in standard drained triaxial test;
- $E_{oed}^{ref}$ , tangent stiffness for primary oedometer loading;
- $E_{ur}^{ref}$ , unloading/reloading stiffness at engineering strains ( $\epsilon = 10^{-3}$  to  $10^{-2}$ );
- $m$ , power for stress-level dependency of stiffness;
- $G_0^{ref}$ , reference shear modulus at very small strains ( $\epsilon < 10^{-6}$ );
- $\gamma_{0.7}$ , shear strain at which  $G_s = 0.722G_0$ .

Brinkgreve et al. [32] published correlations between all of the above mentioned stiffness parameters and the relative density  $R_e$ . These correlations are summarised below ( $p_{ref} = 100$  kPa):

$$E_{50}^{ref} = 60000 \cdot \frac{R_e}{100} \quad [\text{kPa}] \quad (5.20)$$

$$E_{oed}^{ref} = 60000 \cdot \frac{R_e}{100} \quad [\text{kPa}] \quad (5.21)$$

$$E_{ur}^{ref} = 180000 \cdot \frac{R_e}{100} \quad [\text{kPa}] \quad (5.22)$$

$$m = 0.7 - \frac{R_e}{320} \quad [-] \quad (5.23)$$

$$G_0^{ref} = 60000 + 68000 \cdot \frac{R_e}{100} \quad [\text{kPa}] \quad (5.24)$$

$$\gamma_{0.7} = \left(2 - \frac{R_e}{100}\right) \cdot 10^{-4} \quad [-] \quad (5.25)$$

Wichtmann et al. [39] also published a correlation between  $G_0^{ref}$  and  $R_e$ . But instead of a linear relation as presented above, the following relation was given:

$$G_0^{ref} = A_D \cdot \frac{1 + R_e/100}{(a_D - R_e/100)^2} \cdot p_{ref}^{1-n_D} \cdot p^{n_D} \quad (5.26)$$

where  $A_D = 177,000$ ,  $a_D = 17.3$ ,  $n_D = 0.48$  and  $p = p_{ref}$ . A correlation between the void ratio  $e$  and the reference shear modulus  $G_0^{ref}$  is provided by the Material Models Manual from PLAXIS [29] and Benz et al. [40] and is shown below:

$$G_0^{ref} = 33,000 \cdot \frac{(2.97 - e)^2}{1 + e} \quad [\text{kPa}] \quad (5.27)$$

### 5.3.5 Strength

The strength related properties of the model (effective angle of internal friction,  $\phi'$ , effective cohesion,  $c'$ , angle of dilatancy,  $\psi$ , tension cut-off,  $\sigma_t$ , and failure ratio,  $R_f$ ) were defined as given below:

$$\phi' = 28 + 12.5 \frac{R_e}{100} \quad [^\circ], [32] \quad (5.28)$$

$$c' = 0.0 \text{ kPa} \quad (5.29)$$

$$\psi = \phi' - 30 \quad [^\circ], [32] \quad (5.30)$$

$$\sigma_t = 0.0 \text{ kPa} \quad (5.31)$$

$$R_f = 1 - \frac{R_e}{800} \quad [32] \quad (5.32)$$

## 5.4 Earthquake loading

The model was subjected to two different loads: an earthquake with a moment magnitude  $M_w = 6.5$ , and one with  $M_w = 7.5$ . The first earthquake loading corresponded to the horizontal accelerations in EW direction from the 1976 Friuli Italy-01 event, measured at the Codroipo station and identified in the PEER ground motion database [41] by the Record Sequence Number (RSN) 122. The second earthquake loading was the horizontal acceleration record in EW direction from the 1999 Kocaeli event, measured at the Atakoy station in Turkey. This earthquake was identified as RSN 1149 in the PEER ground motion database [41].

The accelerations were introduced in the model by means of prescribed horizontal accelerations at the bottom of the model. Figure 5.6 shows the input accelerations, together with their frequency domain and the corresponding displacements.

## 5.5 Boundary conditions

During the dynamic calculation the default fixities of the model boundaries were switched off for the lateral boundaries, and a tied-degree of freedom boundary condition was introduced. This means that the nodes on the left side were connected to the corresponding nodes on the right side, i.e. when one of the two moved, the other one moved exactly the same. [42]

At the bottom of the model, the boundary condition 'None' was introduced as a representation of the bedrock (bedrock itself was thus not simulated). This boundary condition

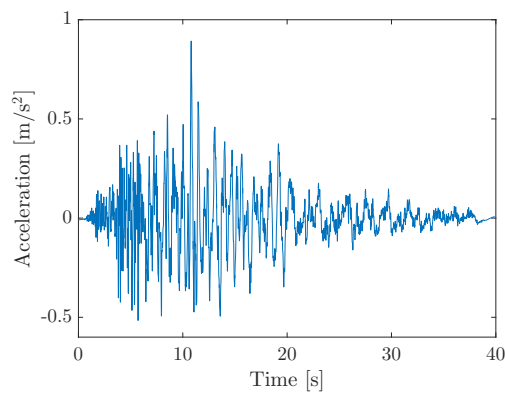
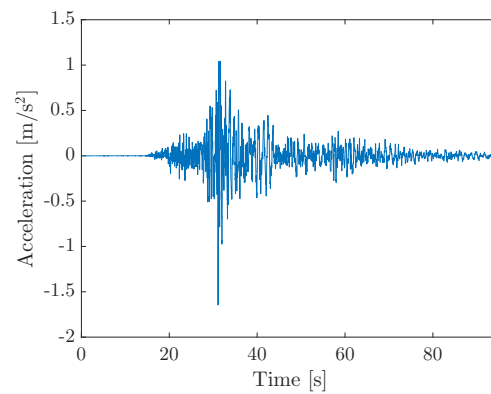
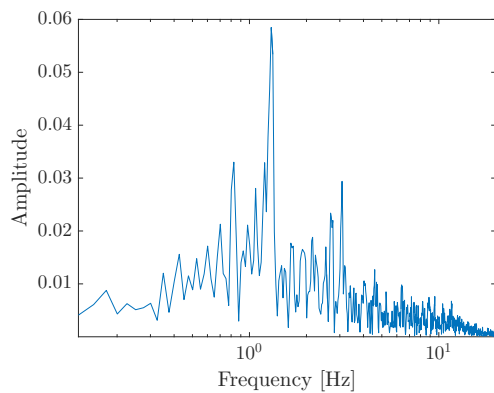
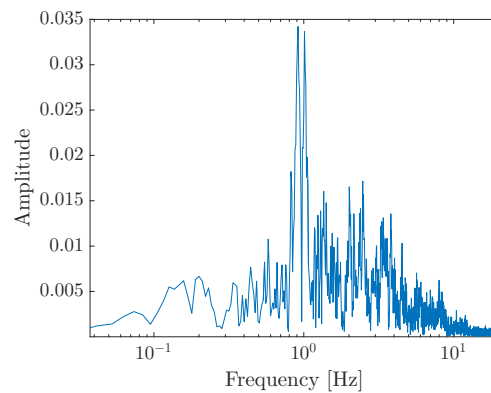
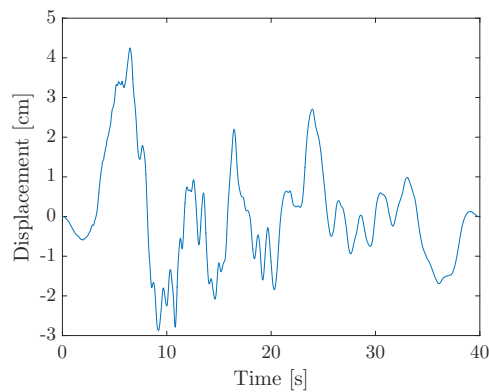
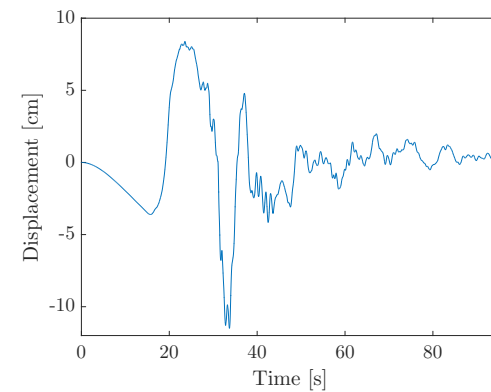
(a)  $M_w = 6.5$ , accelerations(b)  $M_w = 7.5$ , accelerations(c)  $M_w = 6.5$ , frequency domain of accelerations(d)  $M_w = 7.5$ , frequency domain of accelerations(e)  $M_w = 6.5$ , displacements(f)  $M_w = 7.5$ , displacements

Figure 5.6: Earthquake data

causes a full reflection of vertically propagating waves and was thus a good representation of underlying bed rock beneath the sand layer. [28]

## 5.6 Mesh and staged construction

The mesh of the model was obtained by generating a medium mesh in PLAXIS without enhanced mesh refinements. Figure 5.7 shows the meshed model. In PLAXIS the simulation

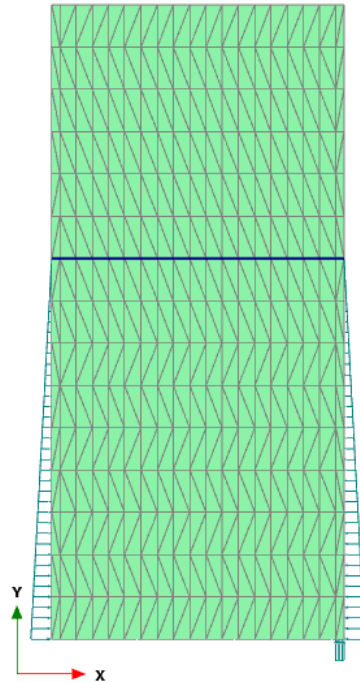


Figure 5.7: Meshed model

of a model always starts with an initial phase in which the initial stresses are calculated. For the uncompacted model this was very easy and the default values could be kept. For the compacted model, however, because of the different  $K_0$ 's no initial equilibrium state could be found by PLAXIS. Therefore the vertical boundaries between the different zones were set as fixed in  $x$ -direction. This way equilibrium was reached in the initial phase, with the intended horizontal and vertical stresses. Off course these fixed zone boundaries had to be released before the earthquake load was applied. This was done in a second phase in which nothing but the release of these fixities happened. The final stage was then used to apply the earthquake loading.

## 6 Liquefaction assessment

It is not possible to simulate real liquefaction in PLAXIS with the HSsmall model. Therefore the assessment of liquefaction had to be done in an other way. The first method used volumetric strain,  $\epsilon_v$ , to assess the possibility for liquefaction. Because liquefaction occurs through the build up of excess pore pressures, which are in turn induced by contractant behaviour of the soil (negative volumetric strain in PLAXIS), this method could give a good indication on whether or not liquefaction was possible. This method was based on the fact that more negative volumetric strains give rise to higher pore pressures making the soil more prone to liquefaction then less negative volumetric strains. Positive volumetric strains or dilatant behaviour will cause suction in undrained conditions making it impossible for the soil to liquefy. This method does however, not allow to determine whether liquefaction actually occurs or not and only gives an indication.

The other way of assessing the liquefaction risk used the procedure suggested by Youd et al. [43] in the summary report from the 1996 NCEER and 1998 NCEER/NSF workshops on evaluation of liquefaction resistance of soils (further named the NCEER method). The procedure given in this report and explained below consists of the calculation of two parameters: the cyclic stress ratio (*CSR*) and the cyclic resistance ratio (*CRR*). The *CSR* is a way of expressing the load acting on the soil due to seismic activity. The *CRR* is a means to express the capacity of the soil to resist this seismic load. In contrast to the method based on volumetric strains, the NCEER method is able to tell whether liquefaction will occur or not by means of a factor of safety against liquefaction *FS*.

### 6.1 Cyclic stress ratio

Following equation shows how to calculate the *CSR*:

$$CSR = \frac{\tau_{av}}{\sigma'_{v0}} = 0.65 \cdot \frac{a_{max}}{g} \cdot \frac{\sigma_{v0}}{\sigma'_{v0}} \cdot r_d \quad (6.1)$$

where  $\tau_{av}$  is the average cyclic shear stress,  $a_{max}$  is the peak horizontal acceleration at the ground surface generated by the earthquake,  $g$  is the acceleration due to gravity (9.81 m/s<sup>2</sup>),  $\sigma_{v0}$  and  $\sigma'_{v0}$  are the total and effective vertical stresses, respectively, and  $r_d$  is the stress reduction coefficient. The latter was hereby calculated as:

$$r_d = 1.0 - 0.00765z \quad \text{for } z \leq 9.15\text{m} \quad (6.2)$$

$$r_d = 1.174 - 0.0267z \quad \text{for } 9.15 < z \leq 23\text{m} \quad (6.3)$$

where  $z$  is the depth below ground surface in meters.

In equation 6.1 all parameters were either constants or known based on the input parameters given in section 5.3, except for the maximum horizontal surface acceleration  $a_{max}$ . The value for the latter was obtained from the simulation results in PLAXIS.

## 6.2 Cyclic resistance ratio

To assess the liquefaction resistance of the soil, the procedure based on a cone penetration test was utilised. The same CPT result as calculated in section 5.2 was used. However, the tip resistance  $q_c$  was normalised in a slightly different way to obtain the normalised and dimensionless cone penetration resistance  $q_{c1N}$ :

$$q_{c1N} = C_n \cdot \frac{q_c}{p_a} \quad (6.4)$$

The correction factor for grain characteristics  $K_c$  allowed to take into account the fines content of the soil and to calculate the clean-sand equivalent normalised cone penetration resistance  $(q_{c1N})_{cs}$ :

$$(q_{c1N})_{cs} = K_c \cdot q_{c1N} \quad (6.5)$$

where

$$K_c = 1.0 \quad \text{for } I_c \leq 1.64 \quad (6.6)$$

$$K_c = -0.403I_c^4 + 5.581I_c^3 - 21.63I_c^2 + 33.75I_c - 17.88 \quad \text{for } I_c > 1.64 \quad (6.7)$$

The cyclic resistance ratio at a magnitude  $M_w = 7.5$ ,  $CRR_{7.5}$ , could then be calculated as follows:

$$CRR_{7.5} = 0.833 \cdot \frac{(q_{c1N})_{cs}}{1,000} + 0.05 \quad \text{if } (q_{c1N})_{cs} < 50 \quad (6.8)$$

$$CRR_{7.5} = 93 \cdot \left[ \frac{(q_{c1N})_{cs}}{1,000} \right]^3 + 0.08 \quad \text{if } 50 \leq (q_{c1N})_{cs} < 160 \quad (6.9)$$

By multiplying the above calculated cyclic resistance ratio at a magnitude  $M_w = 7.5$  with the appropriate magnitude scaling factor,  $MSF$ , the cyclic resistance ratio for other earthquake magnitudes could be calculated as well. The  $MSF$  was calculated as follows:

$$MSF = \frac{10^{2.24}}{M_w^{2.56}} \quad (6.10)$$

where  $M_w$  is the magnitude of the earthquake for which one wants to calculate the  $CRR$ .

The factor of safety against liquefaction,  $FS$ , for earthquakes with any magnitude could then be calculated as the ratio of resistance ( $CRR_{7.5}$ ) and load ( $CSR$ ) multiplied by the appropriate magnitude scaling factor:

$$FS = \frac{CRR_{7.5}}{CSR} MSF \quad (6.11)$$

## 7 Results

### 7.1 CPT results

Figures 7.1 and 7.2 show the simulated CPT data for each of the 10 soils as calculated in section 5.2. To verify the correlations used to simulate the virtual CPT data the soil

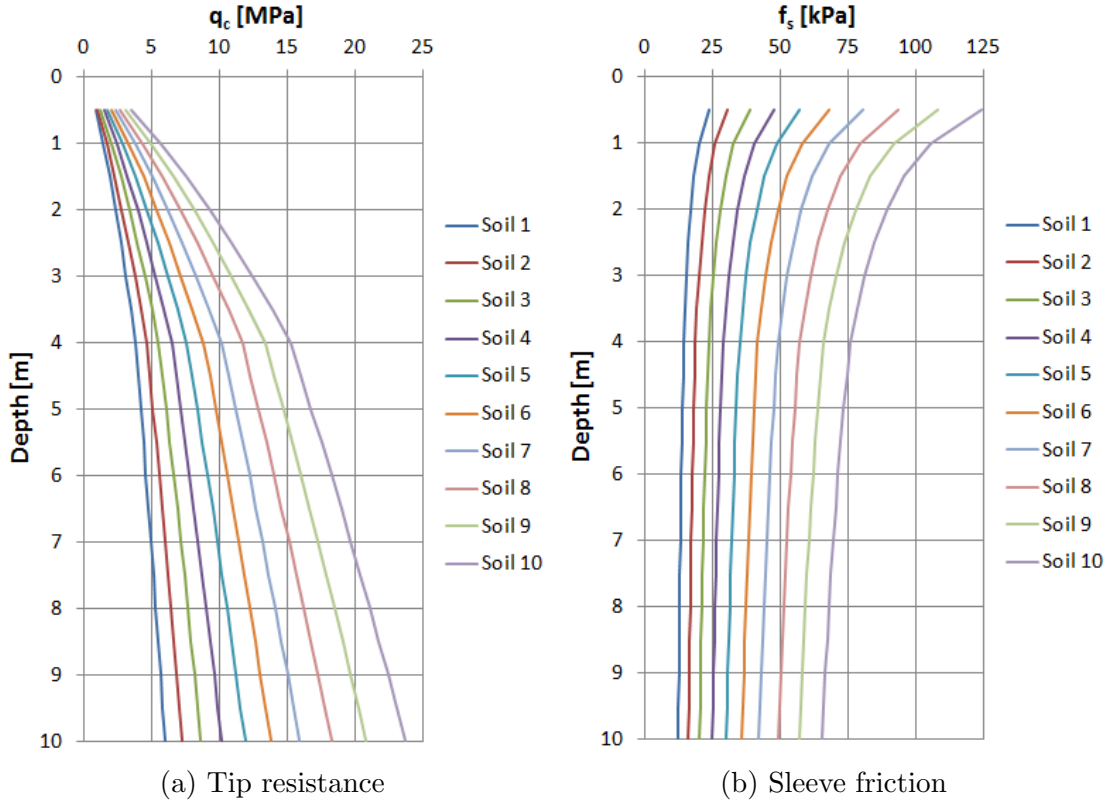


Figure 7.1: Simulated CPT data

behaviour type chart shown in figure 7.3 was used in combination with the above given normalised tip resistance and normalised friction ratio. This indicated that the simulated soil was a sand (clean sand to silty sand, zone 6) – which was exactly what it had to be – and that soil 10 was closer to the ‘dense sand zone’ (zone 7) than soil 9, which in turn was closer to the ‘dense sand zone’ than soil 8, and so forth. Therefore the virtual CPT result was considered to be a good representation of the intended soil. The simulated CPT data for all soils are indicated on figure 7.3 for depths equal to 5 m and 10 m.

An other quick check of the tip resistance  $q_c$  was done by looking at the ratio of the tip resistance of compacted soil and untreated soil. In the case of the virtual CPT this ratio was equal to approximately 4. This is in the range of an increase in  $q_c$  of 300% to 700% measured by Massarsch et al. [11]. This again confirms that the CPT data are reasonable.

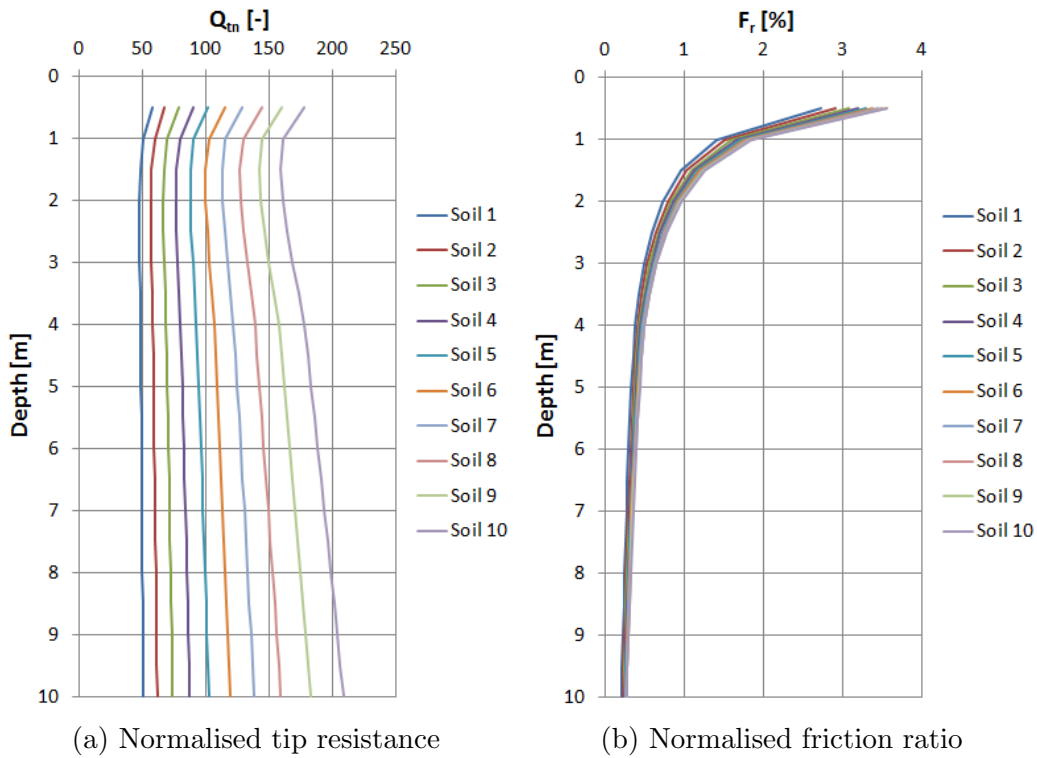
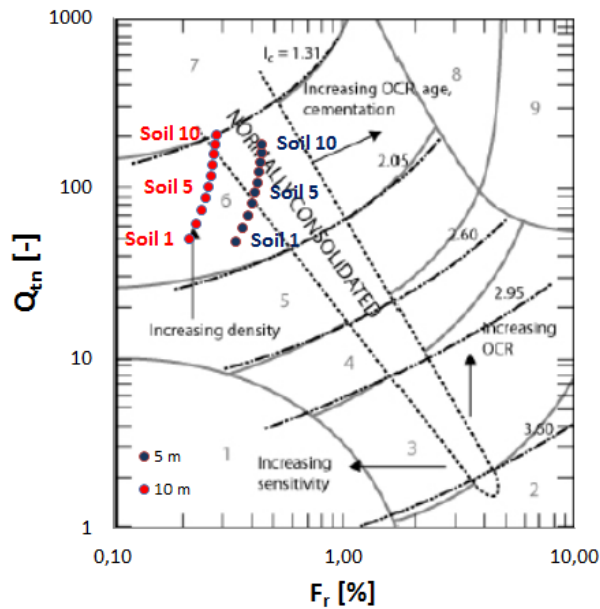


Figure 7.2: Normalised CPT data



| Zone | Soil Behaviour Type                         |
|------|---|
| 1    | Sensitive, fine grained                     |
| 2    | Organic soils - clays                       |
| 3    | Clay - silty clay to clay                   |
| 4    | Silt mixtures - clayey silt to silty clay   |
| 5    | Sand mixtures - silty sand to sandy silt    |
| 6    | Sands - clean sand to silty sand            |
| 7    | Gravelly sand to dense sand                 |
| 8    | Very stiff sand to clayey sand <sup>a</sup> |
| 9    | Very stiff fine grained <sup>a</sup>        |

<sup>a</sup>Heavily overconsolidated or cemented

Figure 7.3: CPT based soil behaviour type chart [25]

## **7.2 Soil parameters**

The parameters used in the numerical model and calculated as in section 5.3 are given in table 7.1.

Table 7.1: Soil parameters

|                  |                      | Loose $\longrightarrow$ Dense |        |        |        |        |         |         |         |         |         |
|------------------|----------------------|-------------------------------|--------|--------|--------|--------|---------|---------|---------|---------|---------|
| Identification   |                      | Soil 1                        | Soil 2 | Soil 3 | Soil 4 | Soil 5 | Soil 6  | Soil 7  | Soil 8  | Soil 9  | Soil 10 |
| $R_e$            | [%]                  | 40.000                        | 43.333 | 46.667 | 50.000 | 53.333 | 56.667  | 60.000  | 63.333  | 66.667  | 70.000  |
| $\gamma_{unsat}$ | [kN/m <sup>3</sup> ] | 16.60                         | 16.73  | 16.87  | 17.00  | 17.13  | 17.27   | 17.40   | 17.53   | 17.67   | 17.80   |
| $\gamma_{sat}$   | [kN/m <sup>3</sup> ] | 19.64                         | 19.69  | 19.75  | 19.80  | 19.85  | 19.91   | 19.96   | 20.01   | 20.07   | 20.12   |
| $e_{init}$       | [-]                  | 0.778                         | 0.764  | 0.749  | 0.735  | 0.721  | 0.706   | 0.692   | 0.678   | 0.663   | 0.649   |
| $e_{min}$        | [-]                  | 0.520                         | 0.520  | 0.520  | 0.520  | 0.520  | 0.520   | 0.520   | 0.520   | 0.520   | 0.520   |
| $e_{max}$        | [-]                  | 0.950                         | 0.950  | 0.950  | 0.950  | 0.950  | 0.950   | 0.950   | 0.950   | 0.950   | 0.950   |
| $E_{50}^{ref}$   | [kPa]                | 24,000                        | 26,000 | 28,000 | 30,000 | 32,000 | 34,000  | 36,000  | 38,000  | 40,000  | 42,000  |
| $E_{oed}^{ref}$  | [kPa]                | 24,000                        | 26,000 | 28,000 | 30,000 | 32,000 | 34,000  | 36,000  | 38,000  | 40,000  | 42,000  |
| $E_{ur}^{ref}$   | [kPa]                | 72,000                        | 78,000 | 84,000 | 90,000 | 96,000 | 102,000 | 108,000 | 114,000 | 120,000 | 126,000 |
| $m$              | [-]                  | 0.5750                        | 0.5646 | 0.5542 | 0.5438 | 0.5333 | 0.5229  | 0.5125  | 0.5021  | 0.4917  | 0.4813  |
| $c'_{ref}$       | [kPa]                | 0                             | 0      | 0      | 0      | 0      | 0       | 0       | 0       | 0       | 0       |
| $\phi'$          | [°]                  | 33.00                         | 33.42  | 33.83  | 34.25  | 34.67  | 35.08   | 35.50   | 35.92   | 36.33   | 36.75   |
| $\psi$           | [°]                  | 3.00                          | 3.42   | 3.83   | 4.25   | 4.67   | 5.08    | 5.50    | 5.92    | 6.33    | 6.75    |
| $\gamma_{0.7}$   | [-]·10 <sup>-6</sup> | 160                           | 157    | 153    | 150    | 147    | 143     | 140     | 137     | 133     | 130     |
| $G_0^{ref}$      | [kPa]                | 87,200                        | 89,467 | 91,733 | 94,000 | 96,267 | 98,533  | 100,800 | 103,067 | 105,333 | 107,600 |
| $OCR$            | [-]                  | 1.000                         | 1.444  | 1.889  | 2.333  | 2.778  | 3.222   | 3.667   | 4.111   | 4.556   | 5.000   |
| $R_f$            | [-]                  | 0.9500                        | 0.9458 | 0.9417 | 0.9375 | 0.9333 | 0.9292  | 0.9250  | 0.9208  | 0.9167  | 0.9125  |
| $\sigma_t$       | [kPa]                | 0                             | 0      | 0      | 0      | 0      | 0       | 0       | 0       | 0       | 0       |

### 7.2.1 Grain size distribution and void ratio

Table 7.2 gives the grain size distribution as shown earlier in figure 5.4. The effective diameter  $D_{10}$  – obtained by linear interpolation – and the diameter marking 60% passage by weight,  $D_{60}$ , were 0.073 mm and 0.260 mm, respectively. From this it followed that the coefficient of uniformity  $C_u$  was equal to 3.586 according to equation 5.15. This, together with the assumed roundness  $R = 0.20$  allowed to read the minimum and maximum void ratio from the diagram shown in figure 5.5. This resulted in  $e_{min}$  and  $e_{max}$  equal to 0.520 and 0.950, respectively.

Table 7.2: Grain size distribution

| Passage [w%] | Grain size [mm] |
|--------------|-----------------|
| 0            | 0.030           |
| 6            | 0.050           |
| 14           | 0.095           |
| 20           | 0.130           |
| 30           | 0.180           |
| 40           | 0.210           |
| 50           | 0.240           |
| 60           | 0.260           |
| 70           | 0.300           |
| 80           | 0.380           |
| 90           | 0.600           |
| 96           | 1.000           |
| 100          | 4.000           |

By means of the suitability number proposed by Brown [10] it could be verified whether the soil was suited to be compacted by means of vibroflotation or not.

$$\text{Suitability number} = 1.7 \sqrt{\frac{3}{D_{50}^2} + \frac{1}{D_{20}^2} + \frac{1}{D_{10}^2}} \quad (7.1)$$

In equation 7.1  $D_{50}$ ,  $D_{20}$  and  $D_{10}$  represent the grain size diameters corresponding to 50%, 20% and 10% passage by weight, respectively. For the proposed grain size distribution, the suitability number turned out to be 29.5. This means that the soil was fairly suited for vibroflotation, as shown in table 7.3

Table 7.3: Soil rating based on the suitability number [10]

| Suitability number | 0 - 10    | 10 - 20 | 20 - 30 | 30 - 50 | >50        |
|--------------------|-----------|---------|---------|---------|------------|
| Rating             | Excellent | Good    | Fair    | Poor    | Unsuitable |

### 7.2.2 Damping

Figure 7.4 shows the shear wave velocity profile and the average value (dashed line) for each soil. Compared to the measurements of Hashash et al. [35], the shear wave velocity profiles were approximately of the same magnitude for the loose soil and for the dense soil, indicating that the created profiles were reasonable. From the average values, the first eigenfrequency  $f_1$  for each soil was calculated using equation 5.18. The eigenfrequencies are given in table 7.4.

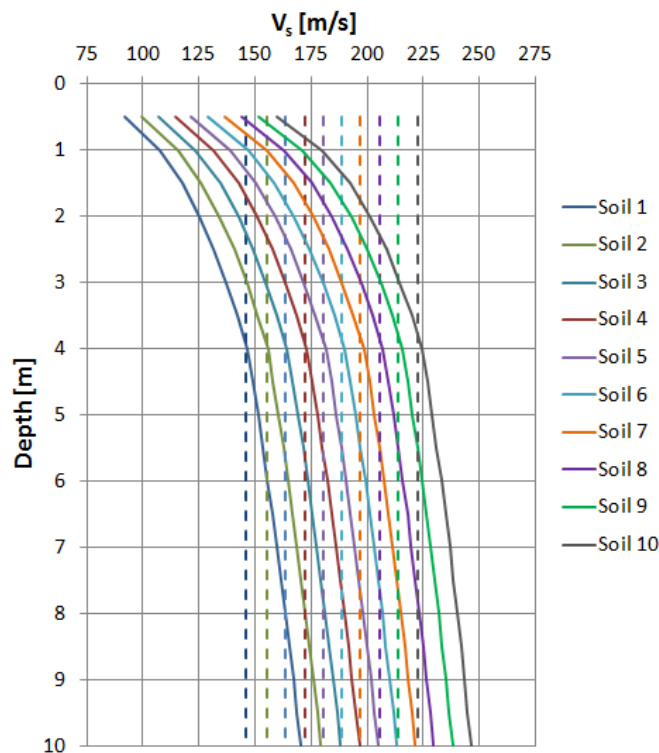


Figure 7.4: Shear wave velocity

Table 7.4: First eigenfrequency and Rayleigh damping coefficients

|         | $f_1$ [Hz] | $\alpha$ | $\beta$             |
|---------|------------|----------|---------------------|
| Soil 1  | 3.65       | 0.2295   | $436 \cdot 10^{-6}$ |
| Soil 2  | 3.88       | 0.2435   | $411 \cdot 10^{-6}$ |
| Soil 3  | 4.09       | 0.2570   | $389 \cdot 10^{-6}$ |
| Soil 4  | 4.30       | 0.2702   | $370 \cdot 10^{-6}$ |
| Soil 5  | 4.51       | 0.2833   | $353 \cdot 10^{-6}$ |
| Soil 6  | 4.72       | 0.2963   | $337 \cdot 10^{-6}$ |
| Soil 7  | 4.92       | 0.3094   | $323 \cdot 10^{-6}$ |
| Soil 8  | 5.13       | 0.3225   | $310 \cdot 10^{-6}$ |
| Soil 9  | 5.34       | 0.3357   | $298 \cdot 10^{-6}$ |
| Soil 10 | 5.56       | 0.3491   | $286 \cdot 10^{-6}$ |

To obtain the second target frequency,  $f_j$ , the dominant frequency from the input earthquake acceleration had to be determined. This was done with the software MATLAB by calculating the Fourier transformation from the earthquake signals (figures 5.6c and 5.6d). The MATLAB code is given in appendix A. The dominant frequencies in the input accelerations for the magnitude 6.5 earthquake and the magnitude 7.5 earthquake were 1.30 Hz and 0.92 Hz, respectively. According to the procedure given by Hudson et al. [38]  $f_j$  was equal to  $f_1$  for both earthquakes since both had dominant frequencies smaller than  $f_1$ . This was the case for each soil.

The damping coefficients  $\alpha$  and  $\beta$  could be obtained by solving equation 5.17. Hereby the damping ratios  $\xi_i$  and  $\xi_j$  were assumed to be equal to 1% [35]. Table 7.4 shows the resulting values for  $\alpha$  and  $\beta$ . Figure 7.5 shows the damping ratio due to the Rayleigh

damping as a function of frequency<sup>3</sup>.

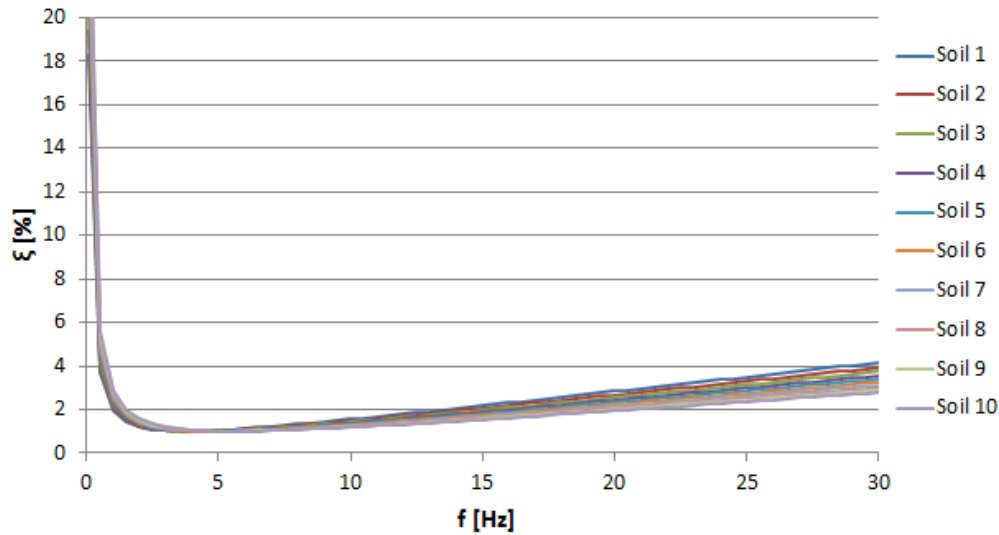


Figure 7.5: Rayleigh damping as a function of frequency

### 7.2.3 Stiffness

Figure 7.6 compares the three relations to obtain the small strain stiffness  $G_0^{ref}$  given in equations 5.24, 5.26 and 5.27. It turned out that all three relations give very similar results, especially in the range used within the simulations (40% to 70%). Combined with the fact that the other stiffness parameters were also obtained by the relations given by Brinkgreve et al. [32], it was chosen by the author to continue with equation 5.24.

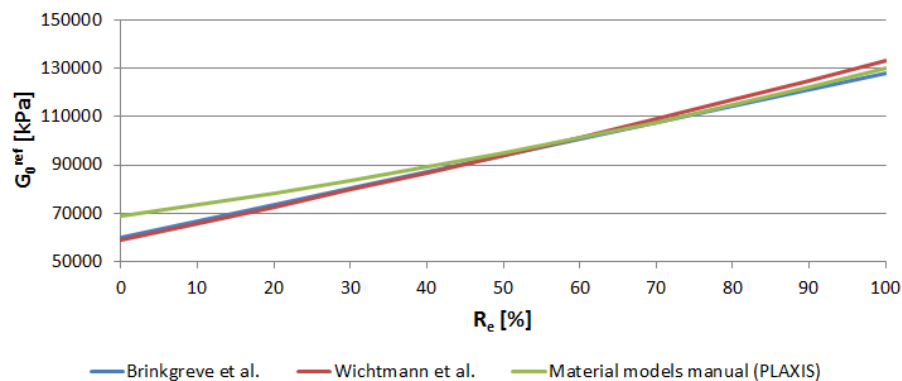


Figure 7.6: Small strain shear modulus as a function of relative density ( $p_{ref} = 100$  kPa)

<sup>3</sup>Strain dependent material damping is inherent to the HSsmall model and is therefore not mentioned separately (section 5.3.3)

### 7.3 Simulation results

Figure 7.7 shows the initial stress state in the uncompacted soil. The total and effective vertical stress,  $\sigma_v$  and  $\sigma_v^{eff}$ , respectively, and the effective horizontal stress  $\sigma_{xx}^{eff}$  are shown from left to right. Figures 7.8 shows the initial stress states in the compacted and average model with a compaction point spacing of 4 m before subjection to an earthquake loading. Figures 7.9 and 7.10 show the initial stress states for the 3.11 m spacing model and the 2.22 m spacing model, respectively.

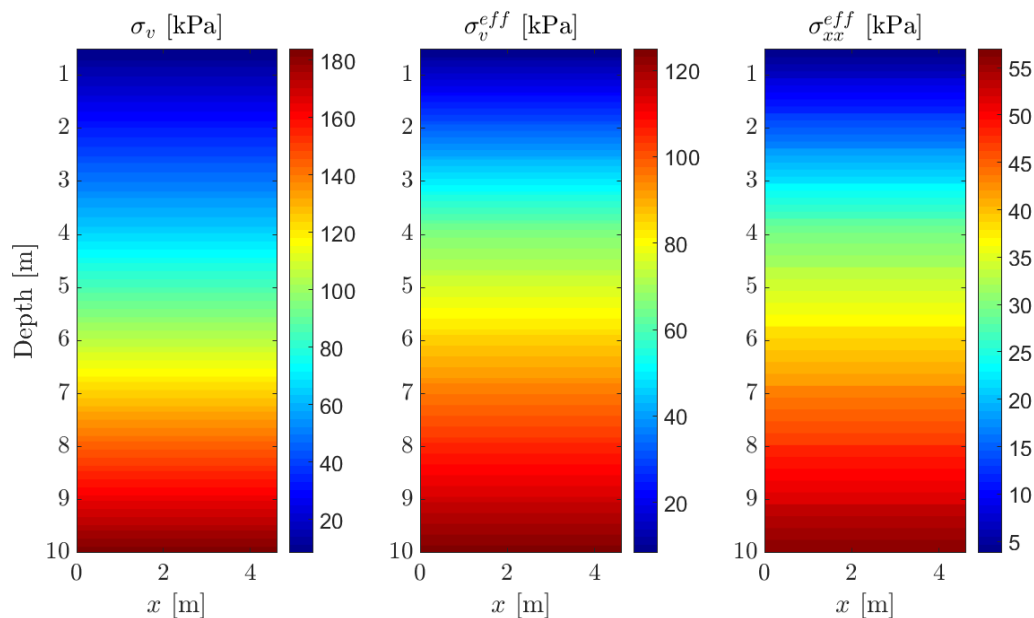
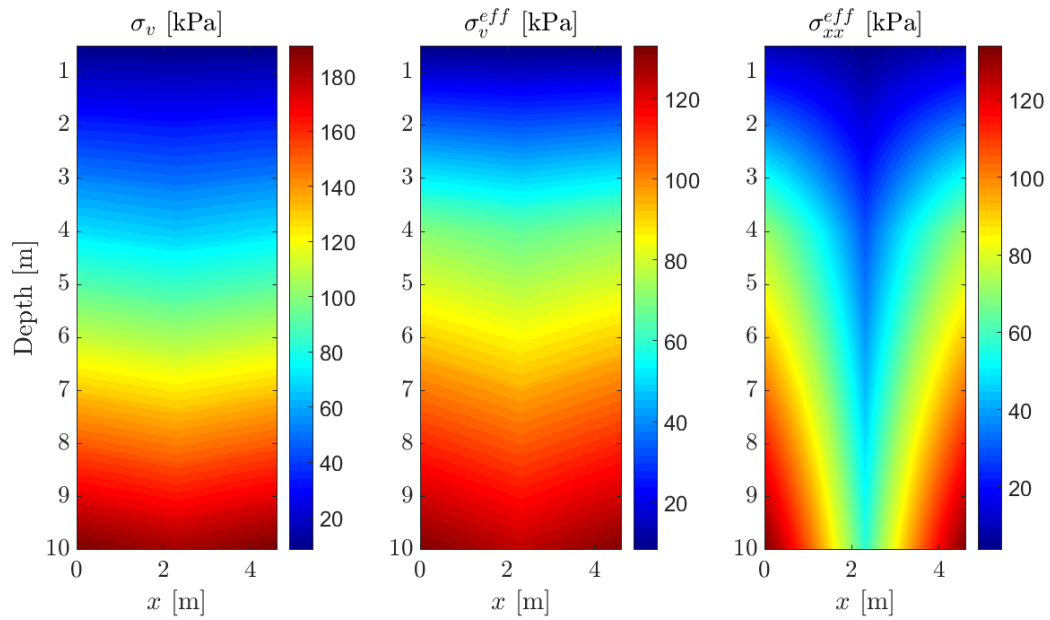


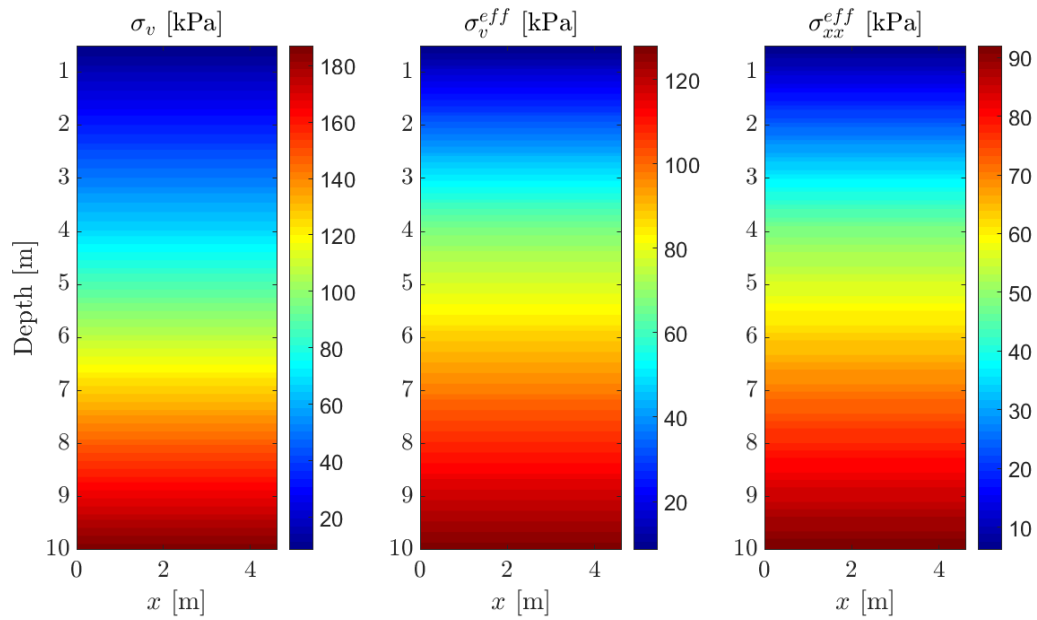
Figure 7.7: Initial stress state in the uncompacted model

As mentioned earlier, the ability of the soil to liquefy was assessed by means of the volumetric strain  $\epsilon_v$ . The volumetric strain was evaluated at six places for each simulation: at two different depths, 7 m and 9 m, and at three different  $x$ -coordinates,  $x = 0$  m,  $x = x_{CPT}$  and  $x = x_{middle}$ .  $x_{CPT}$  represented the  $x$ -coordinate at which contractors generally perform a CPT test to obtain the ‘best’ CPT result and was equal to 1/3 of the spacing between compaction points.  $x_{middle}$  was the  $x$ -coordinate at the middle of the model and corresponds to the position of the least compacted soil in the compaction grid. Table 7.5 shows the  $x$ -coordinates for the different models.

Figure 7.11 shows the variation of  $\epsilon_v$  over time during the magnitude 6.5 earthquake for a compaction point spacing of 4 m. Figure 7.12 shows the same for the magnitude 7.5 earthquake. Figures 7.13 and 7.14 show  $\epsilon_v$  as a function of time with a probe spacing equal to 3.11 m for a magnitude 6.5 and a magnitude 7.5 earthquake, respectively. Figures 7.15 and 7.16 show  $\epsilon_v$  as a function of time with a probe spacing equal to 2.22 m for a magnitude 6.5 and a magnitude 7.5 earthquake, respectively.

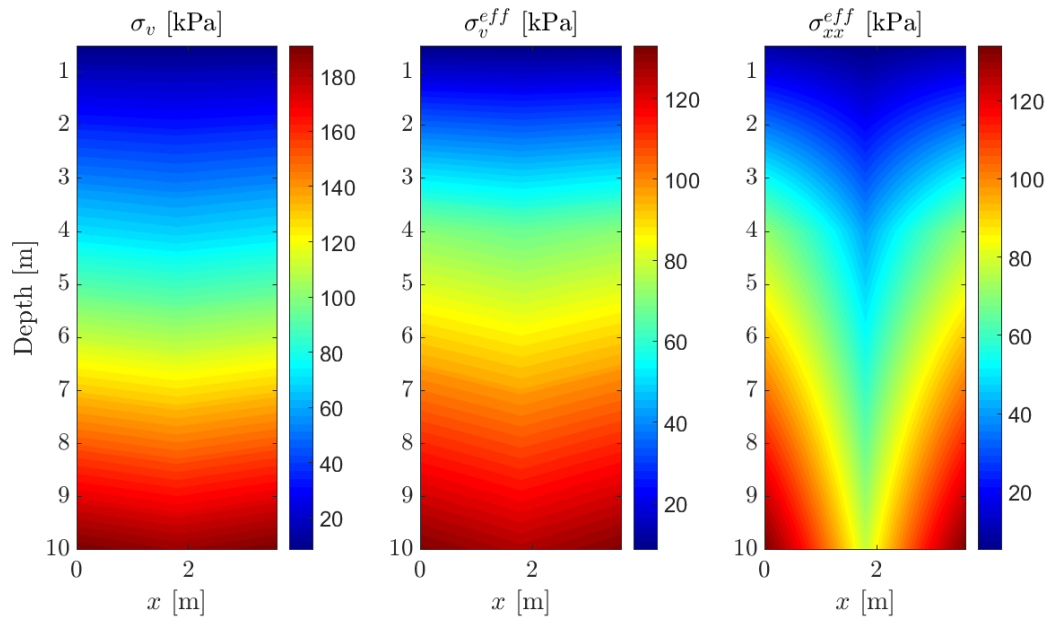


(a) Compacted model

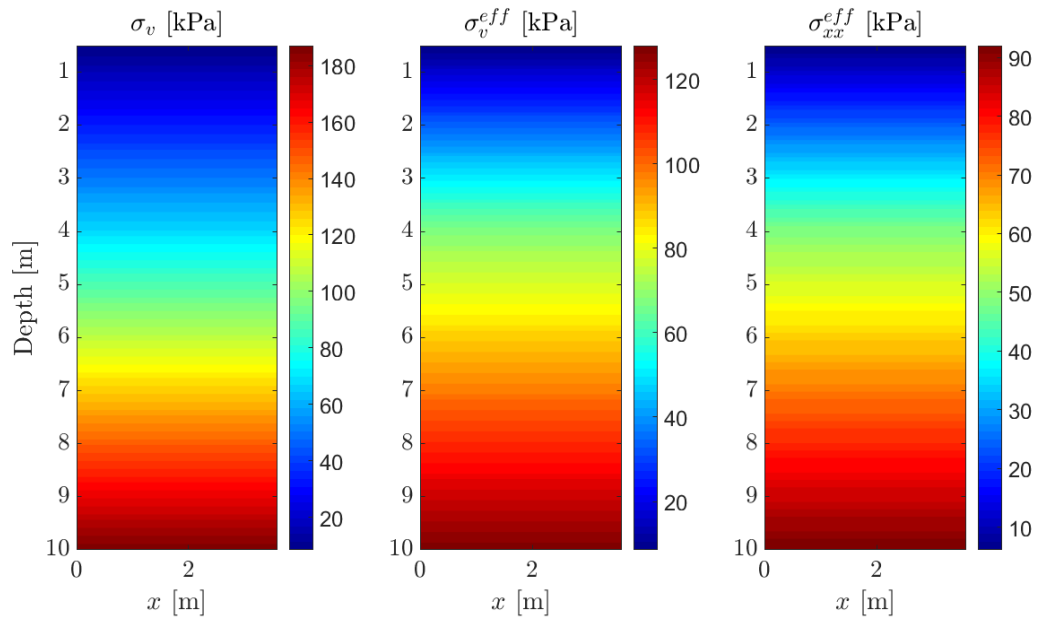


(b) Average model

Figure 7.8: Initial stress states for 4 m probe spacing

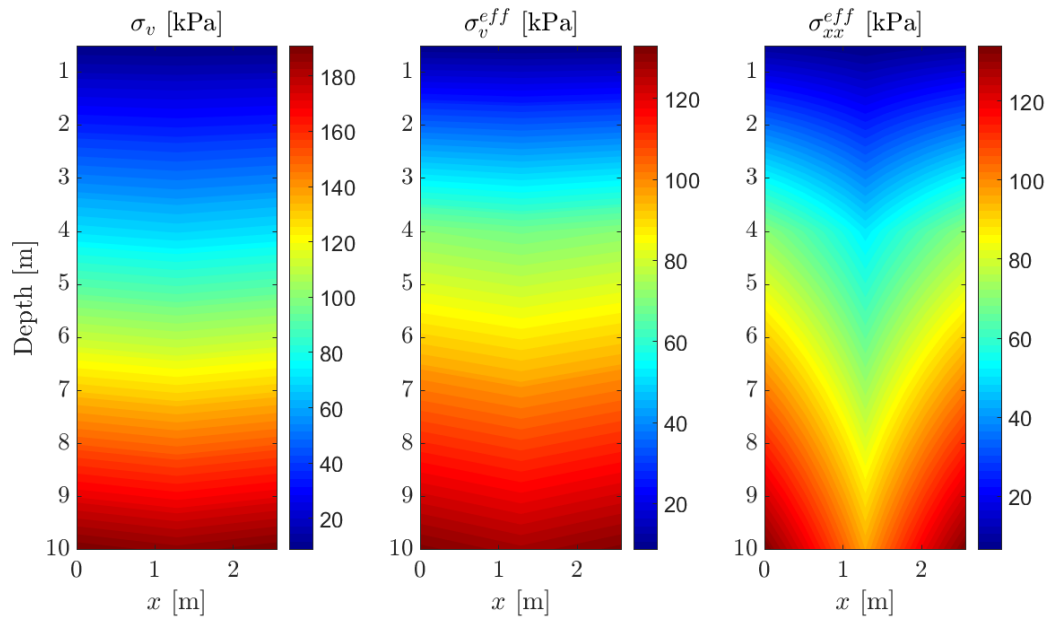


(a) Compacted model

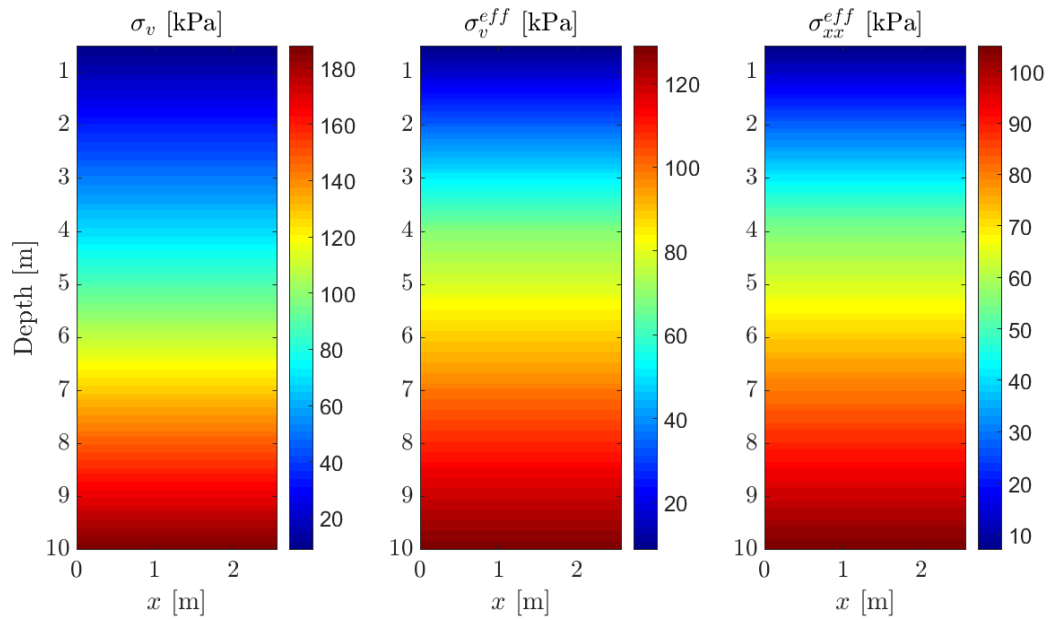


(b) Average model

Figure 7.9: Initial stress states for 3.11 m probe spacing



(a) Compacted model



(b) Average model

Figure 7.10: Initial stress states for 2.22 m probe spacing

Table 7.5: ‘Best’ CPT location and model center

| Spacing [m]      | 4.00 | 3.11 | 2.22 |
|------------------|------|------|------|
| $x_{CPT}$ [m]    | 1.33 | 1.04 | 0.74 |
| $x_{middle}$ [m] | 2.31 | 1.80 | 1.28 |

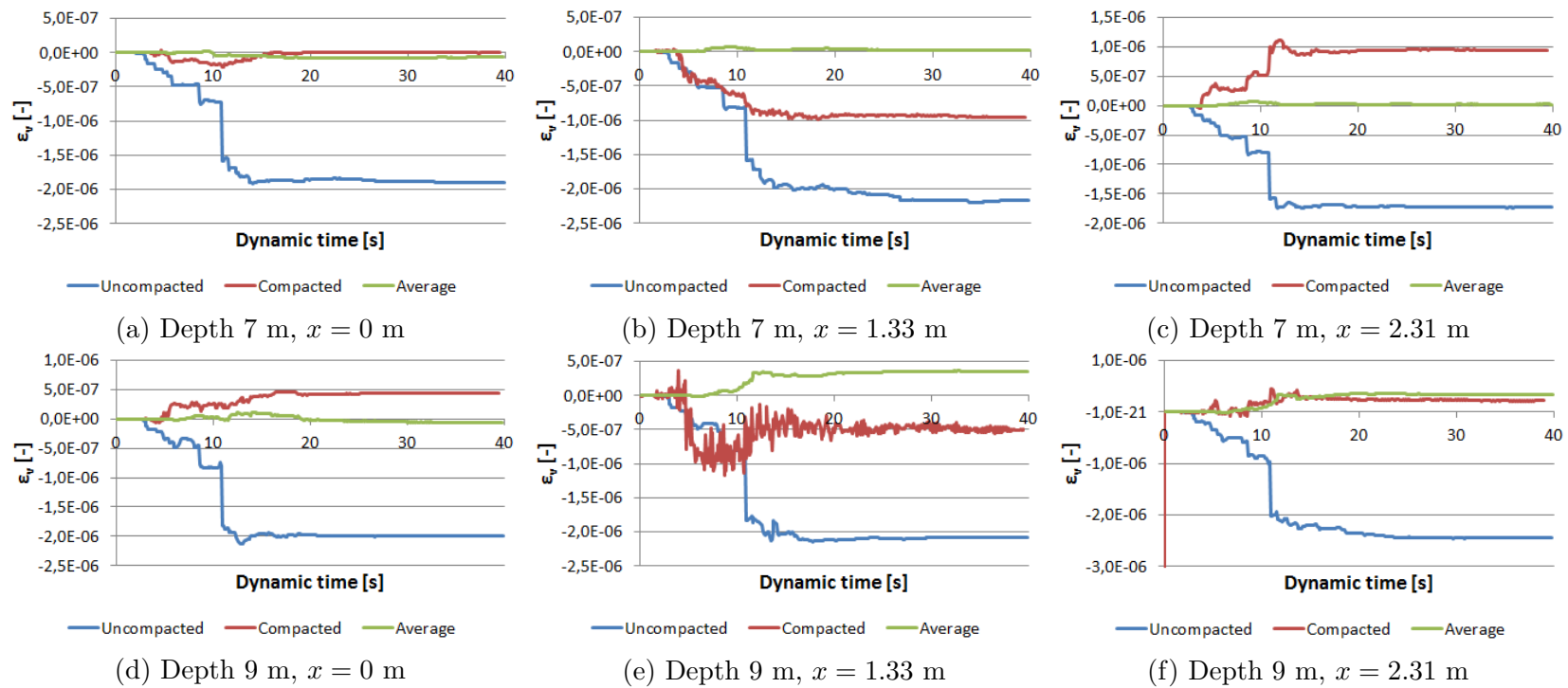


Figure 7.11: Volumetric strains for a probe spacing equal to 4 m, magnitude 6.5

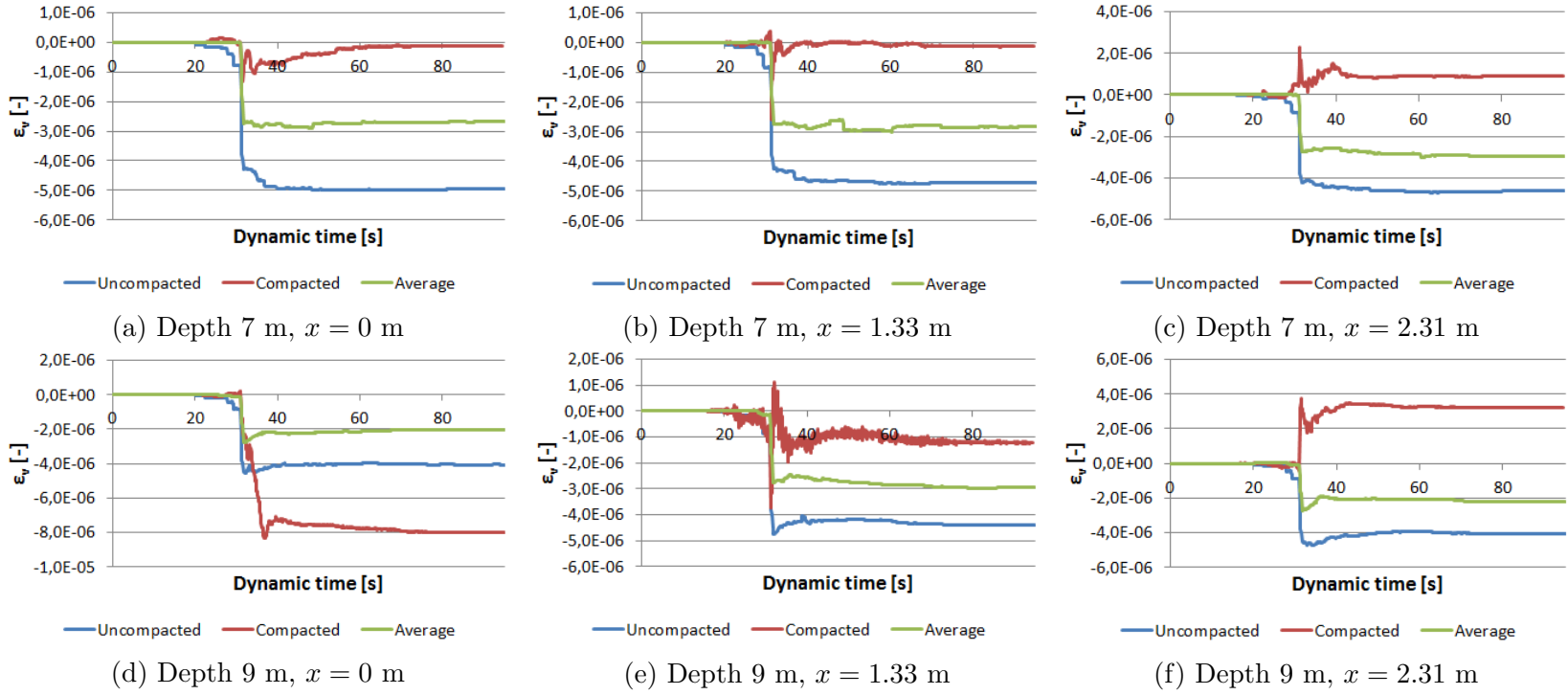


Figure 7.12: Volumetric strains for a probe spacing equal to 4 m, magnitude 7.5

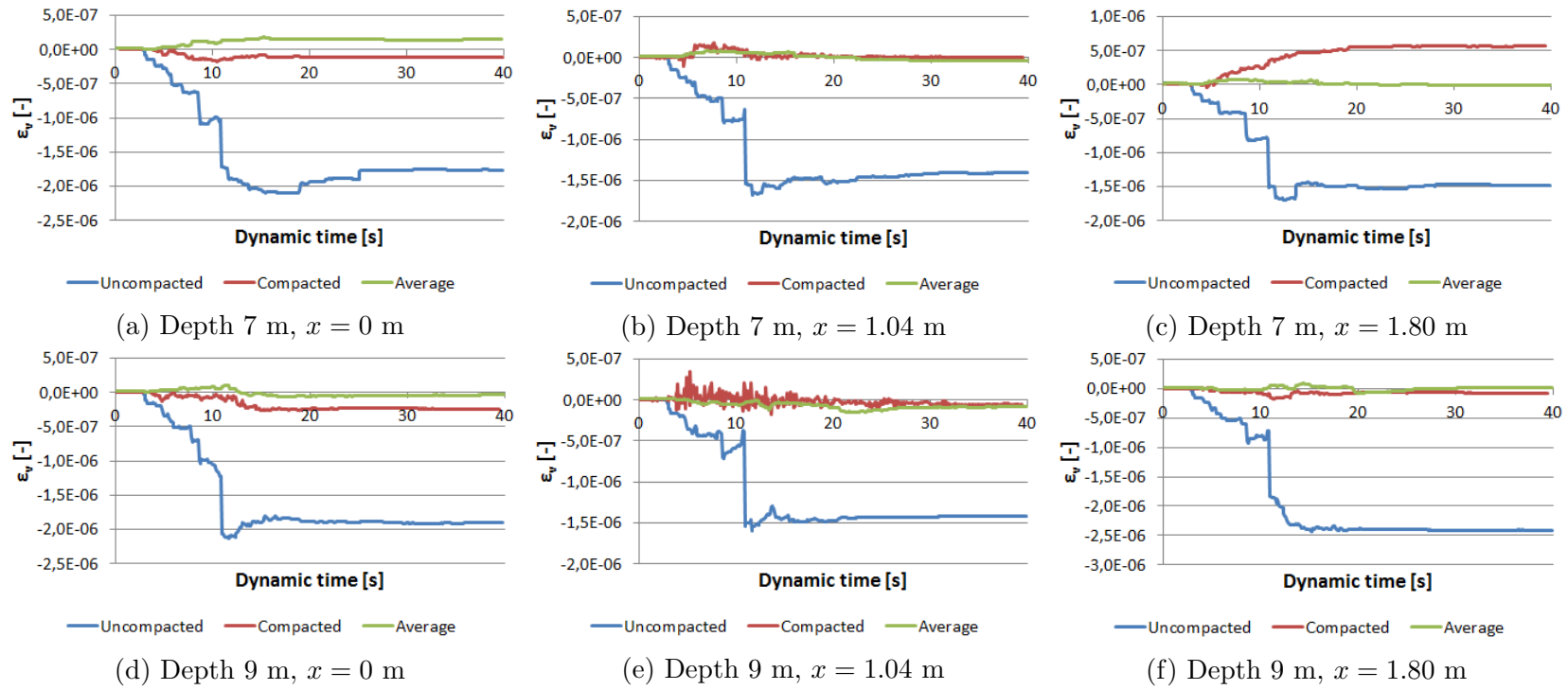


Figure 7.13: Volumetric strains for a probe spacing equal to 3.11 m, magnitude 6.5

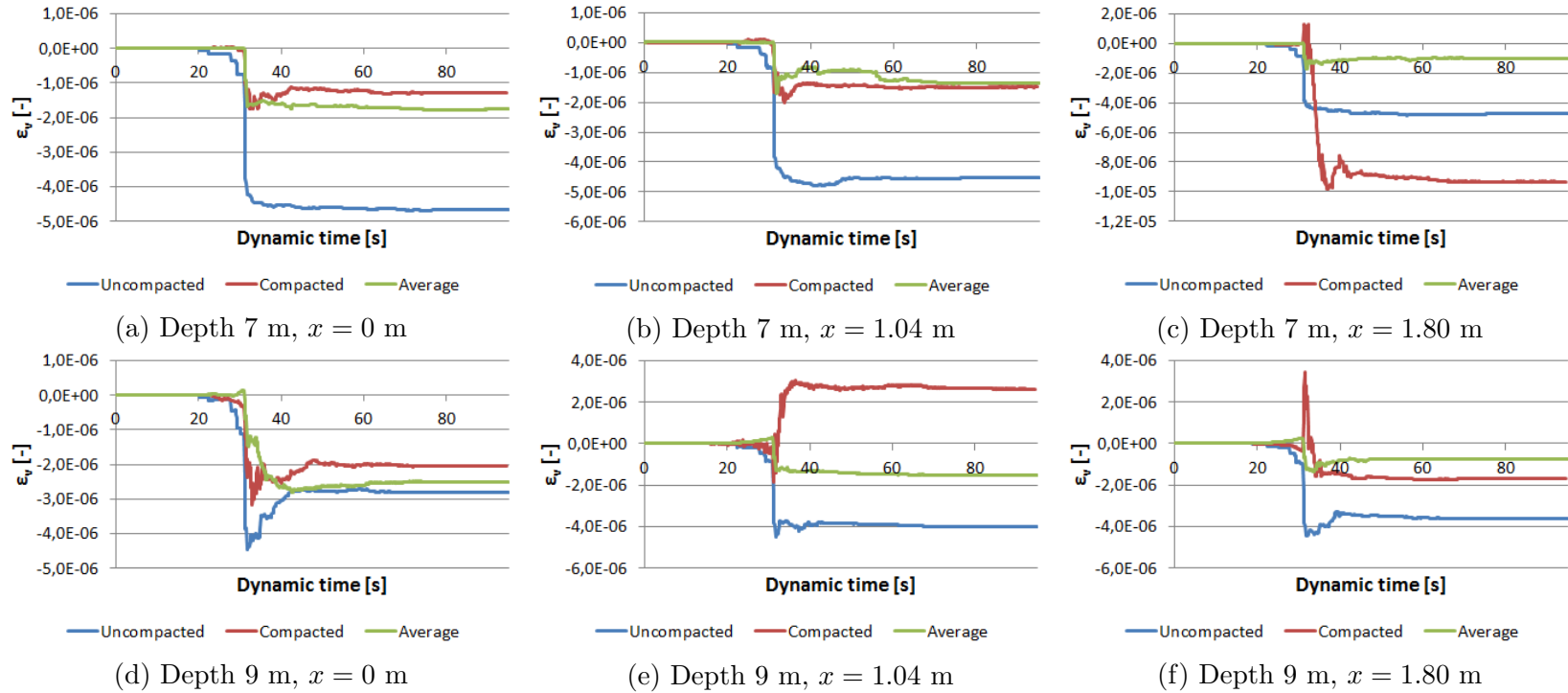


Figure 7.14: Volumetric strains for a probe spacing equal to 3.11 m, magnitude 7.5

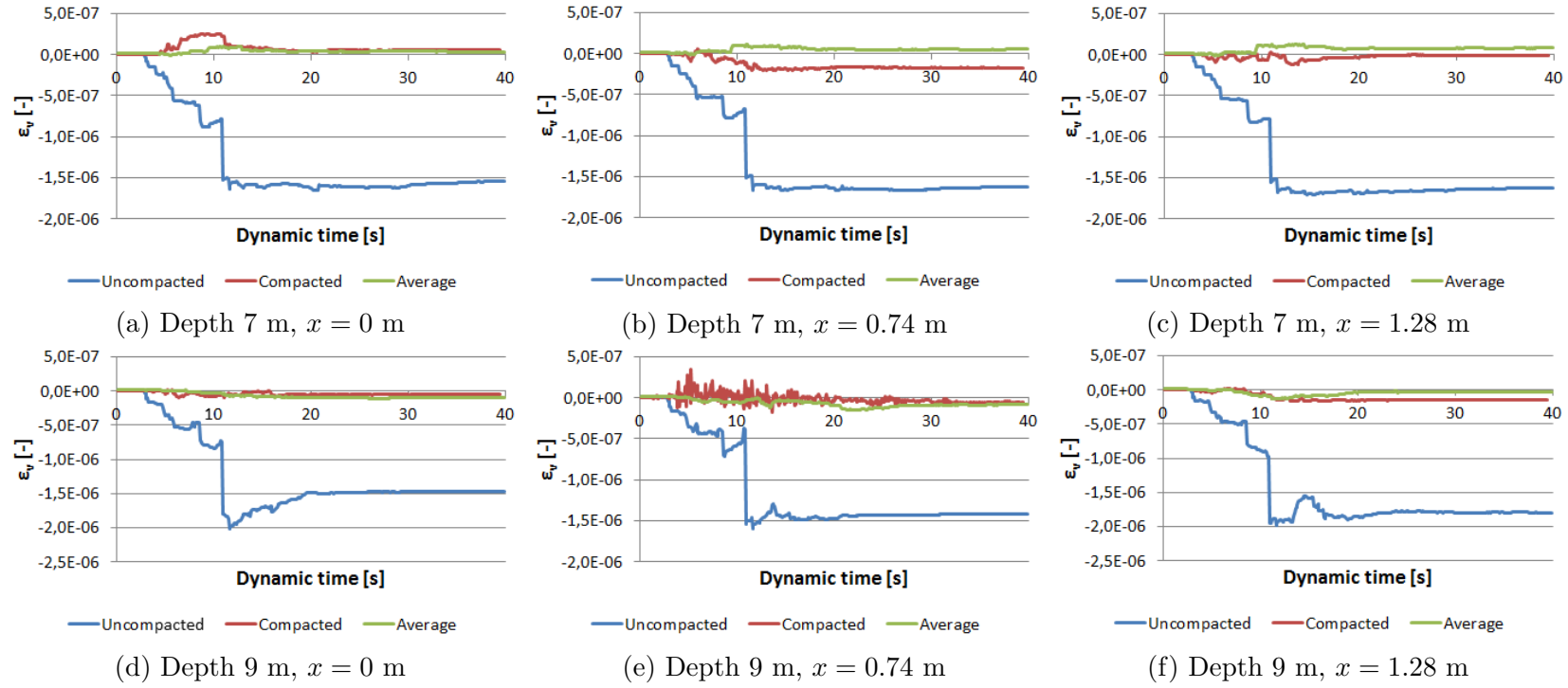


Figure 7.15: Volumetric strains for a probe spacing equal to 2.22 m, magnitude 6.5

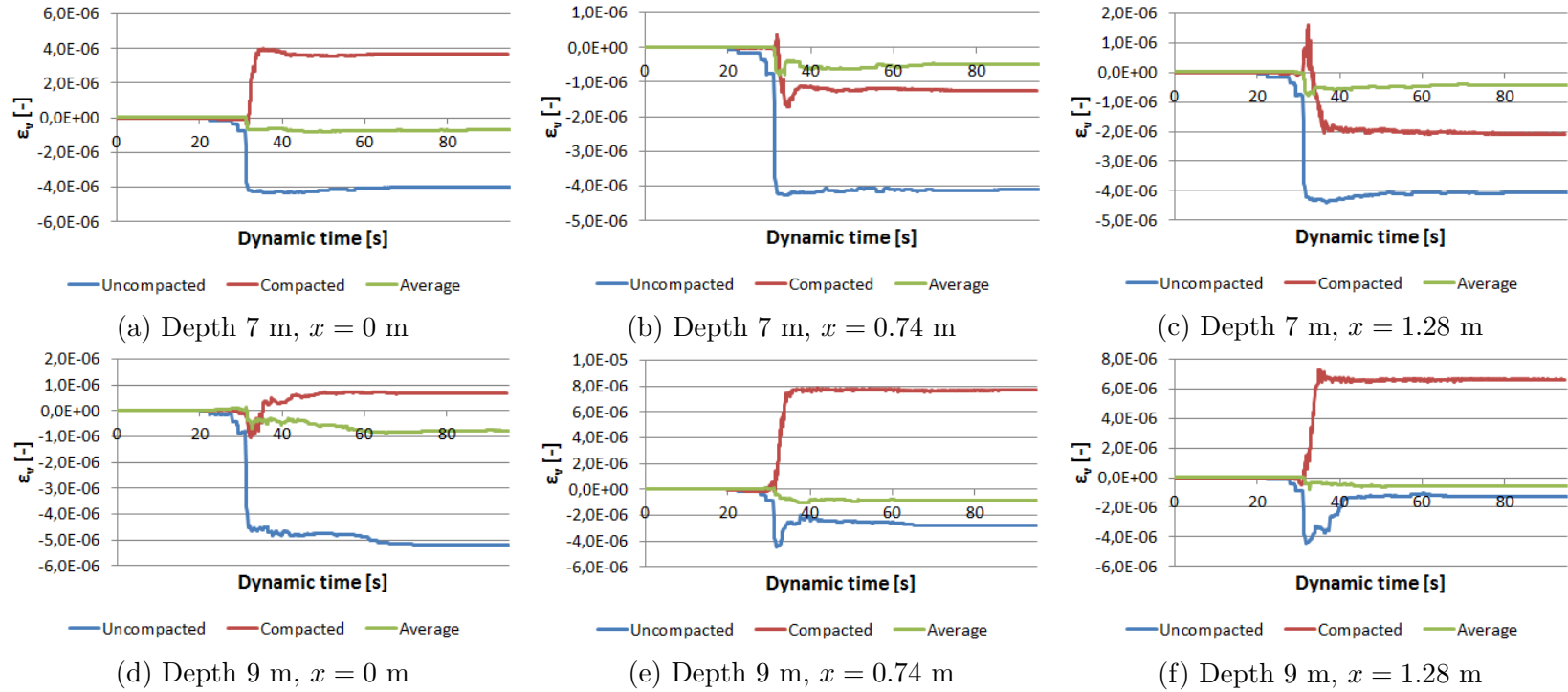


Figure 7.16: Volumetric strains for a probe spacing equal to 2.22 m, magnitude 7.5

## 7.4 Liquefaction assessment

To check the simulation results a liquefaction assessment based on the procedure suggested in Youd et al. [43] and as explained in section 6 was also carried out. Therefore the absolute maximum horizontal surface accelerations  $a_{max}$  produced in the simulations were used. These are shown in figure 7.17.

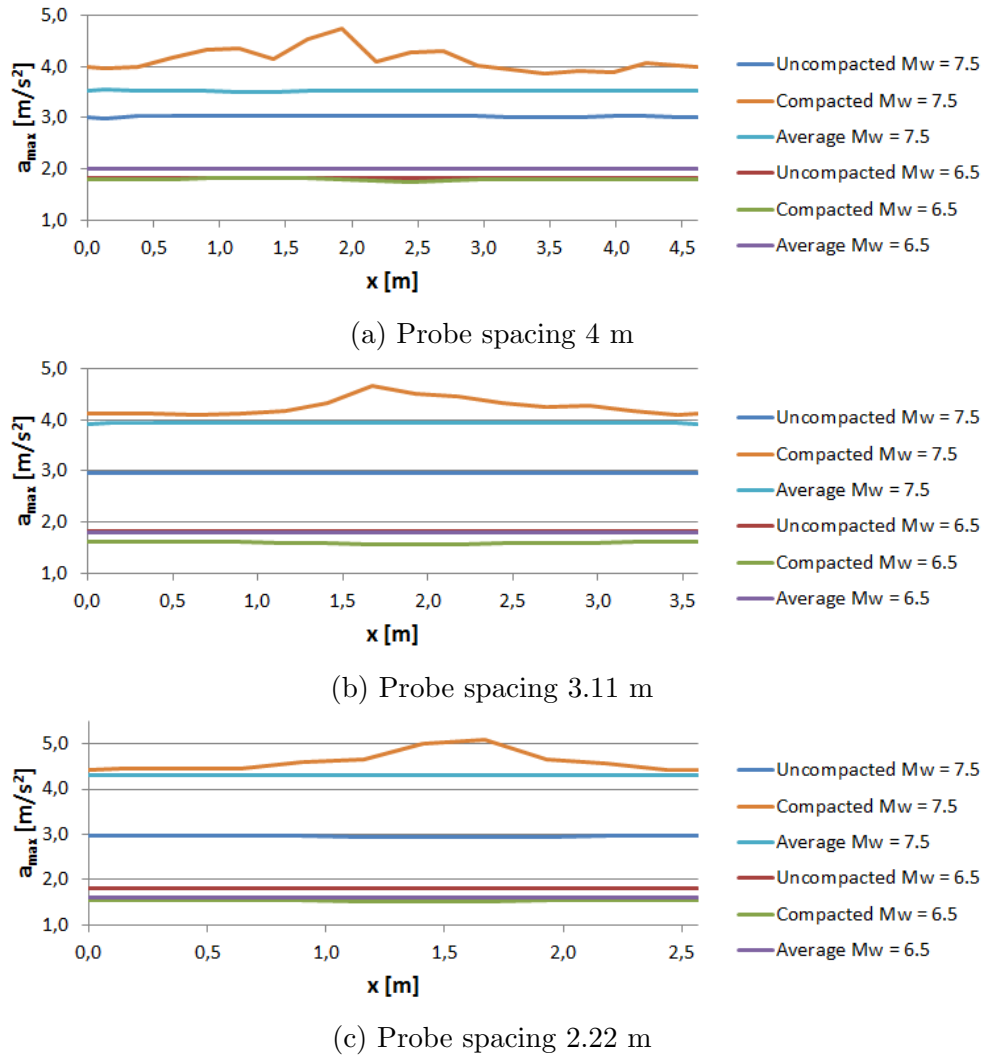
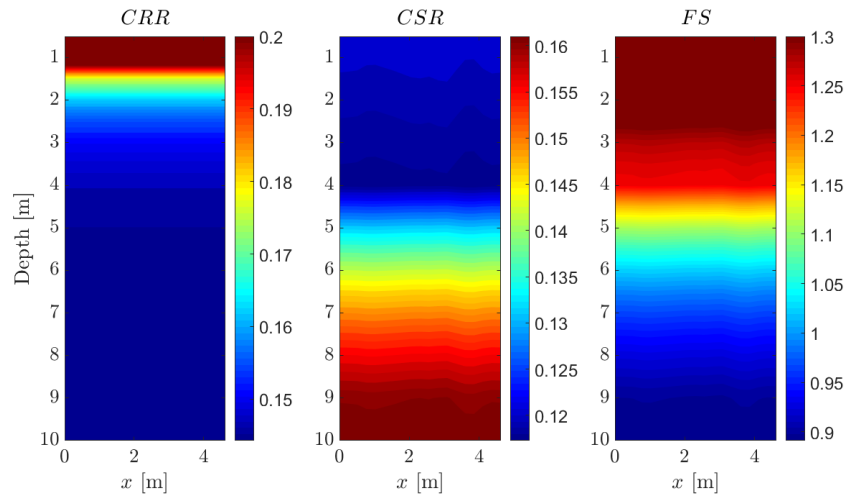
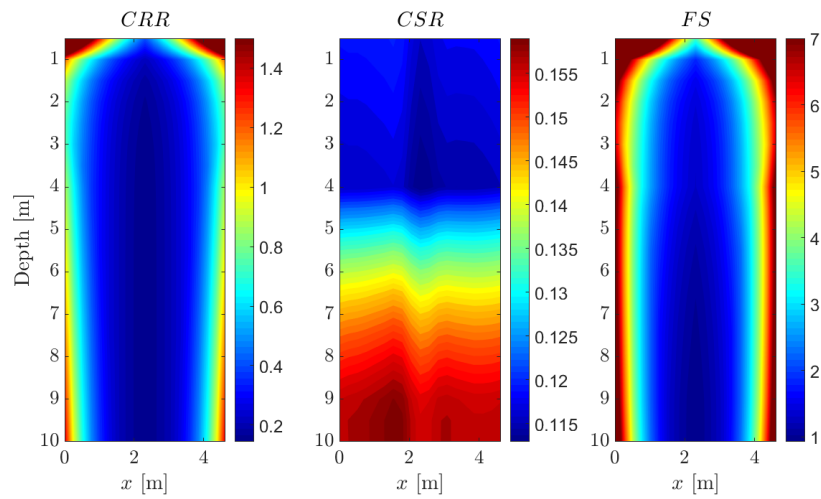


Figure 7.17: Absolute maximum horizontal surface accelerations

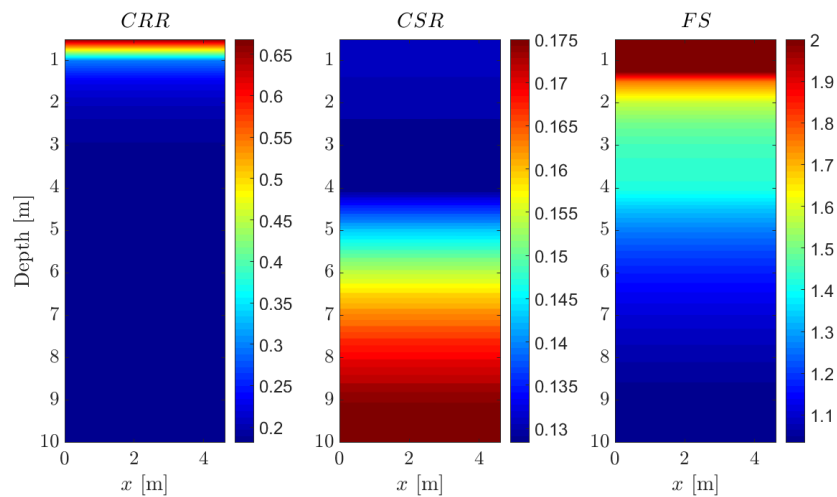
For each simulation,  $CRR$ ,  $CSR$  and  $FS$  were calculated over the width and the depth of the model as explained in section 6. The results are shown in figures 7.18, 7.19, 7.20, 7.21, 7.22 and 7.23.



(a) Uncompact model

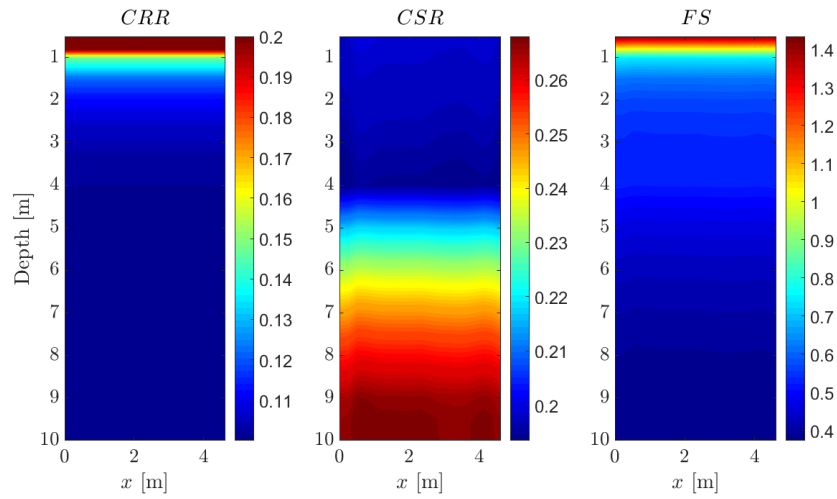


(b) Compacted model

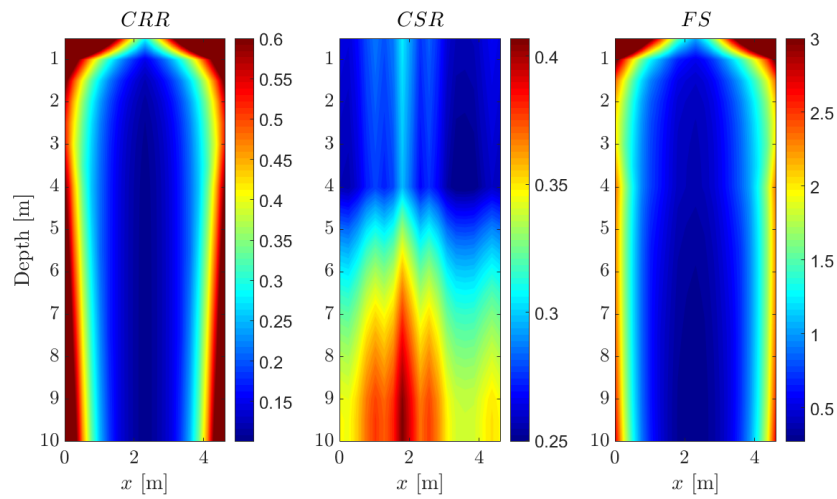


(c) Average model

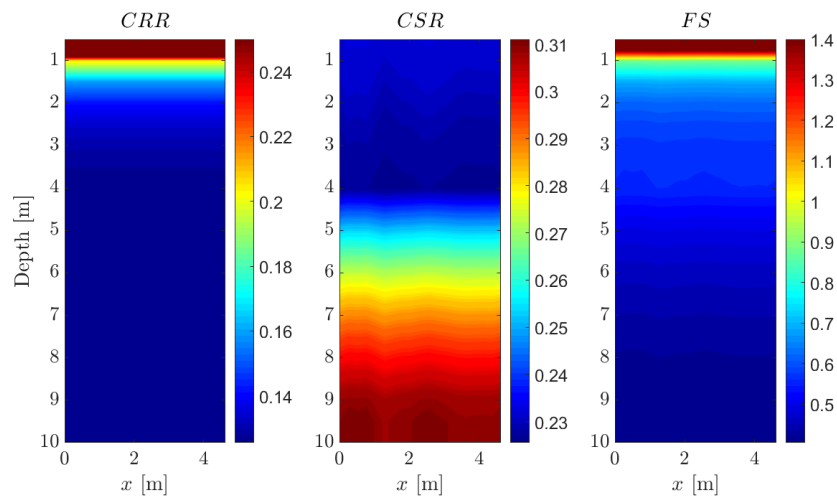
Figure 7.18: *CRR*, *CSR* and *FS* for 4 m probe spacing and  $M_w = 6.5$



(a) Uncompact model

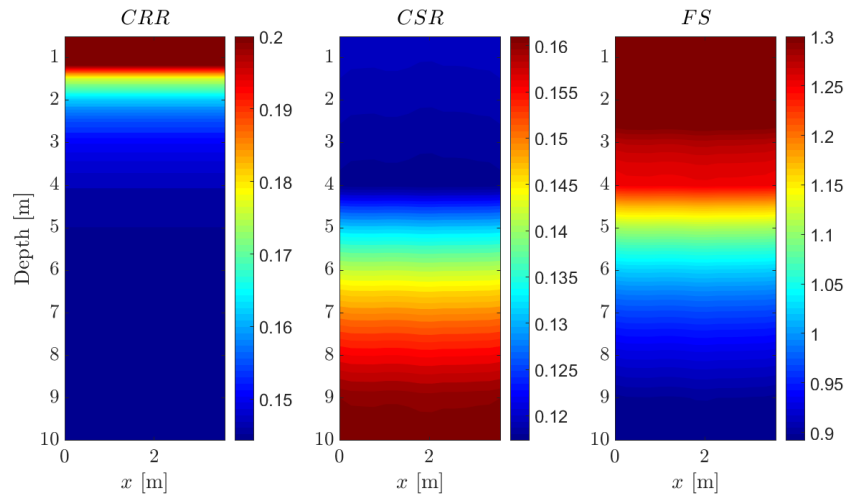


(b) Compacted model

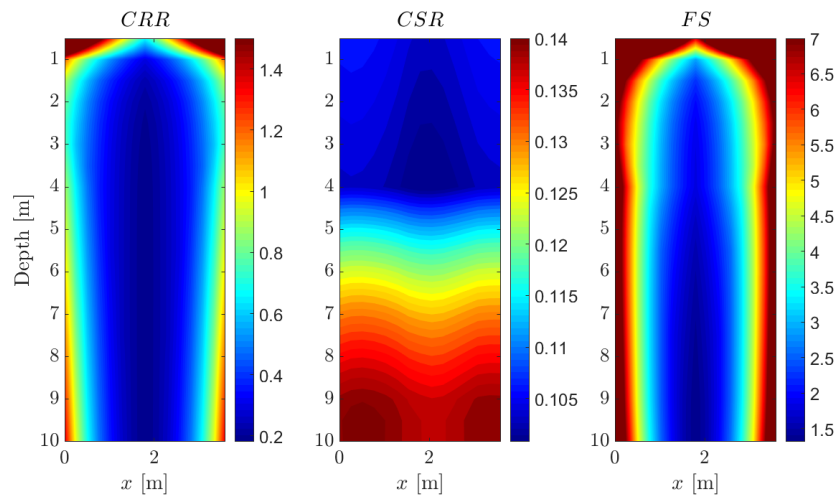


(c) Average model

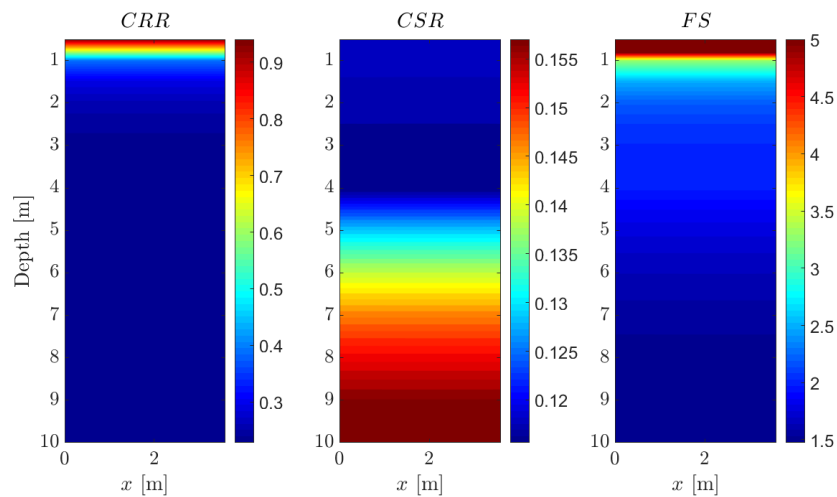
Figure 7.19: *CRR*, *CSR* and *FS* for 4 m probe spacing and  $M_w = 7.5$



(a) Uncompact model

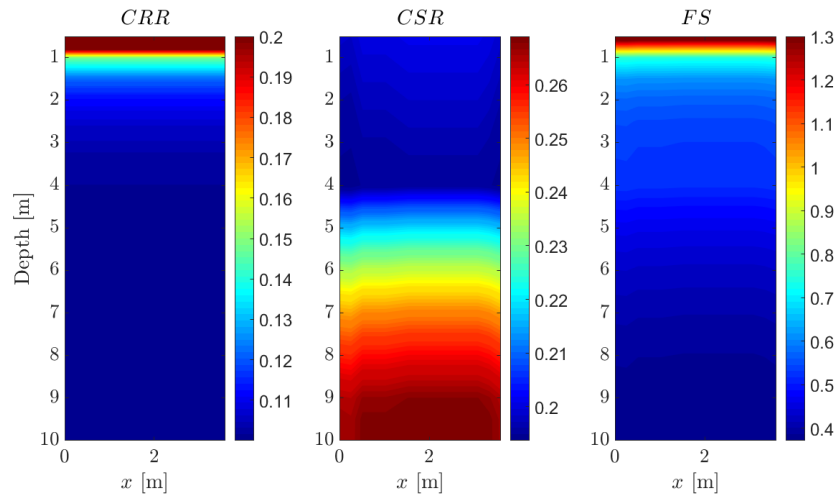


(b) Compacted model

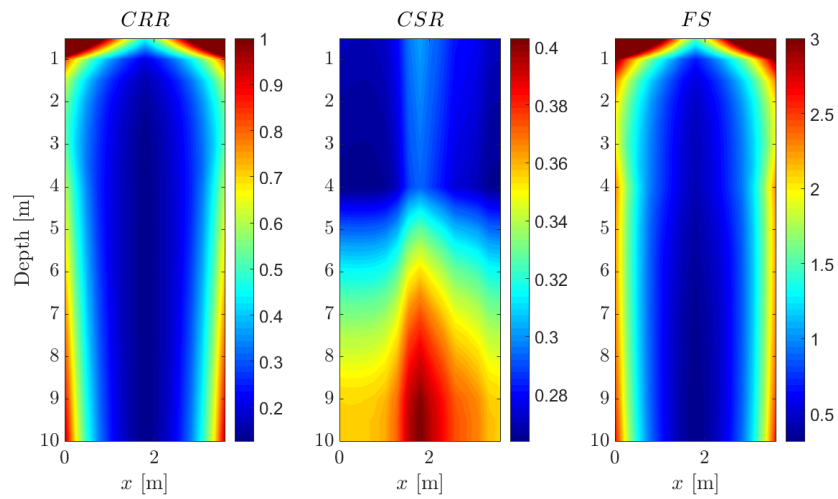


(c) Average model

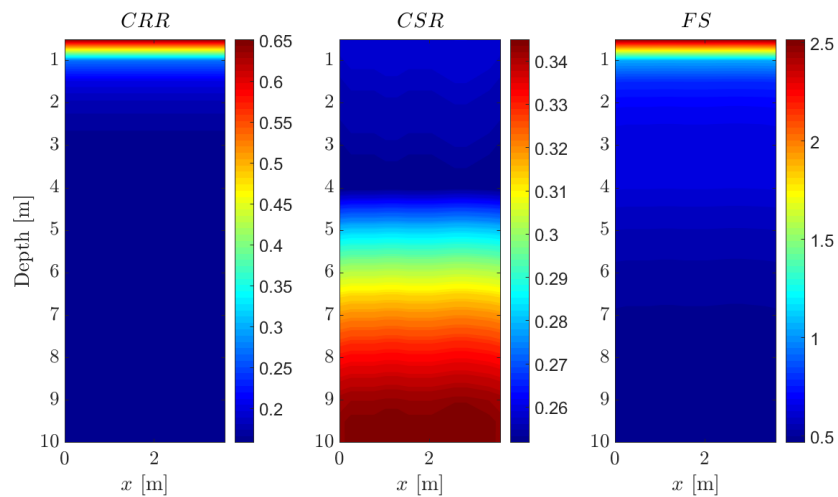
Figure 7.20: *CRR*, *CSR* and *FS* for 3.11 m probe spacing and  $M_w = 6.5$



(a) Uncompact model

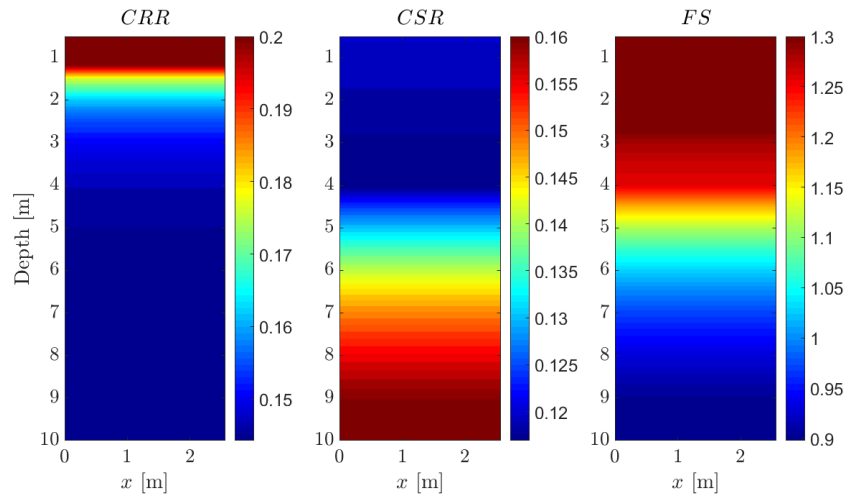


(b) Compacted model

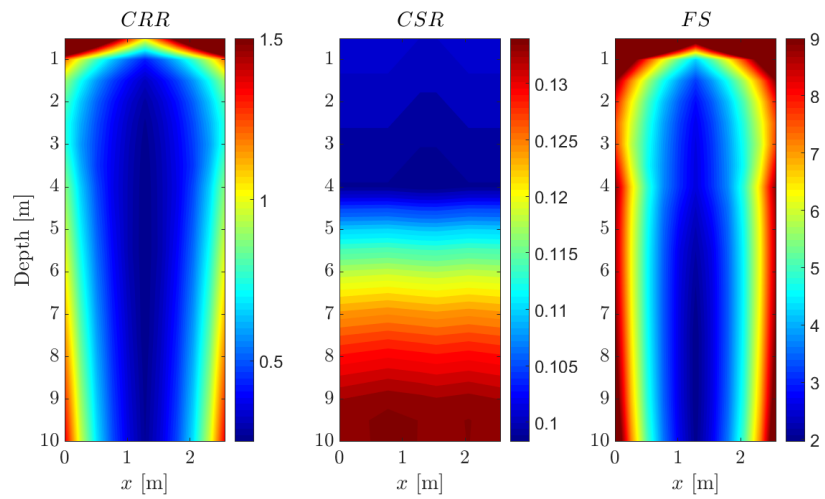


(c) Average model

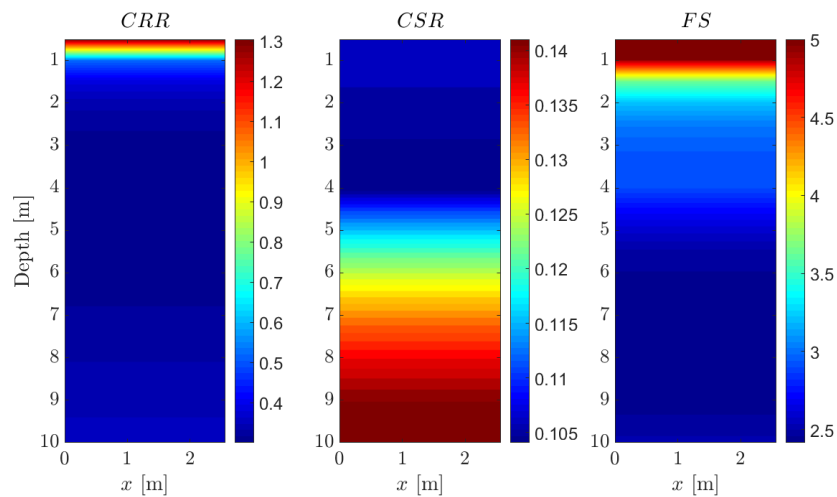
Figure 7.21:  $CRR$ ,  $CSR$  and  $FS$  for 3.11 m probe spacing and  $M_w = 7.5$



(a) Uncompact model

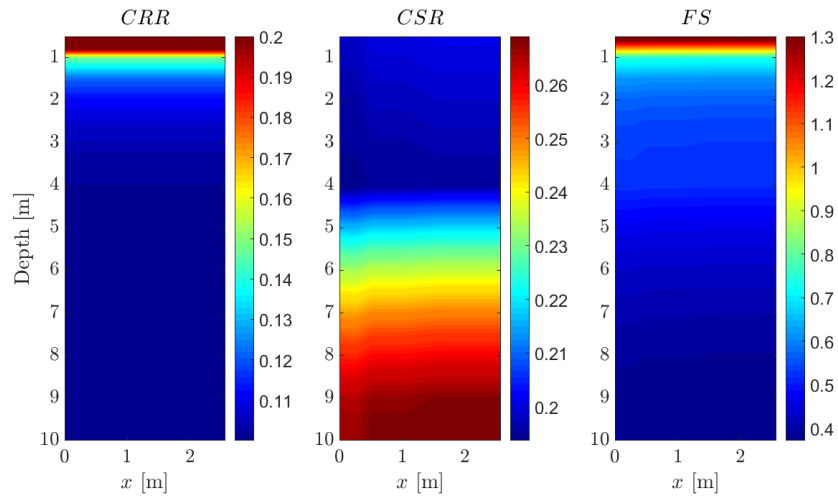


(b) Compacted model

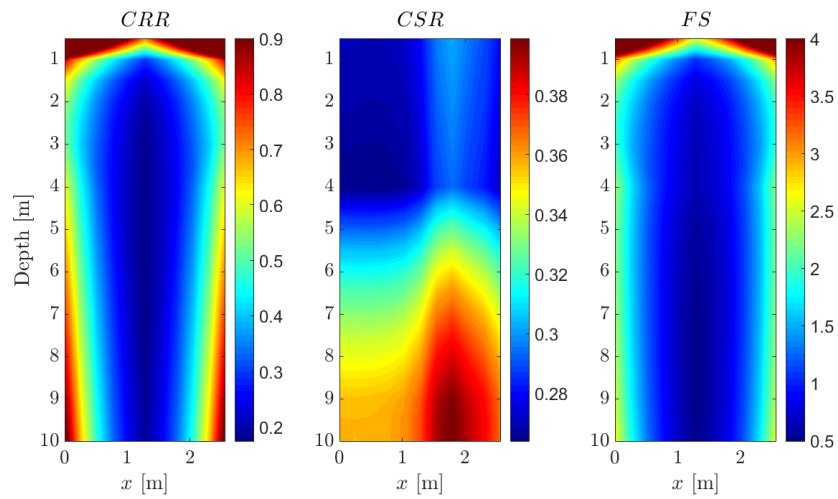


(c) Average model

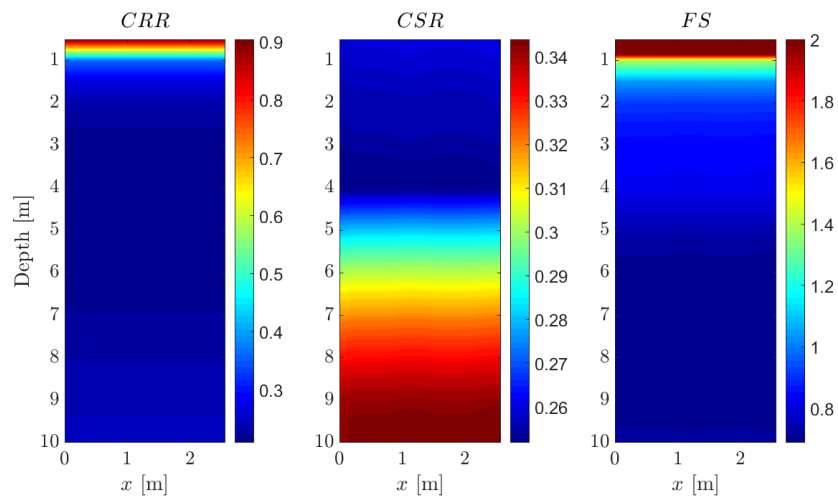
Figure 7.22: *CRR*, *CSR* and *FS* for 2.22 m probe spacing and  $M_w = 6.5$



(a) Uncompact model



(b) Compacted model



(c) Average model

Figure 7.23: *CRR*, *CSR* and *FS* for 2.22 m probe spacing and  $M_w = 7.5$

## 8 Discussion

### 8.1 Simulation results

#### 8.1.1 Initial stresses

When comparing the initial stresses of the compacted and average models (figures 7.8, 7.9 and 7.10) with the initial stresses in uncompact state (figure 7.7), following differences were noticed:

- For both total and effective vertical stresses, V-shaped contours arised after compaction (figures 7.8a, 7.9a and 7.10a). This could simply be explained by the increase in density due to compaction.
- The horizontal stress contours clearly showed the variable horizontal stress across the treated soil, going from high horizontal stress at the compaction point to low horizontal stress at the least compacted point (figures 7.8a, 7.9a and 7.10a).
- Horizontal stresses were higher in the least compacted point for smaller compaction point spacings.
- When looking at the average models (figures 7.8b, 7.9b and 7.10b), there was a slight increase in vertical stress that was logically explained by the slightly higher density of the average soil compared to the uncompact soil.
- The horizontal stresses in the average models were constant over the width of the model and were higher for smaller spacing distances and equal to the average of the horizontal stresses in the soil at  $x_{CPT}$  and  $x_{middle}$  (table 7.5) in the compacted model. This was of course a very rough estimation of reality.

#### 8.1.2 Volumetric strain

Figures 7.11 to 7.16 show the volumetric strain  $\epsilon_v$  as a function of time in the points mentioned earlier. The first observation that could be made was the contractant behaviour of the soil in the uncompact model. This suggested that liquefaction was possible.

In the compacted models, the contractant behaviour of the soil had clearly reduced in almost every point, which indicated that the chance for liquefaction had become less. In some cases the contractant behaviour had even changed in dilatant behaviour making liquefaction impossible to occur (negative excess pore pressures and thus increase in effective stresses which is exactly the opposite of the cause of liquefaction). Few exceptions could be observed, namely in figures 7.12d and 7.14c. In these two cases the compacted model shows an even stronger contractant behaviour than the uncompact model. This might indicate local liquefaction. This, however, can not be said with full certainty since PLAXIS is not able to simulate liquefied soil. In some cases it could also be observed that the soil behaved more dilatant (or less contractant) in the zone with less compaction. These

counter-intuitive results could not be explained by the author and might be explained by further research.

Comparing the average model results to the compacted model results, it seemed that the average model only approximated the compacted model well for the smaller earthquake ( $M_w = 6.5$ ) and for smaller spacing distances (3.11 m and 2.22 m) which can be seen in figures 7.13 and 7.15. However, for the heavier earthquake ( $M_w = 7.5$ ) the average model seemed to underestimate the volumetric strains (figures 7.12, 7.14 and 7.16), and if so, taking the average model as an approximation for the heterogeneous site conditions would be on the safe side.

## 8.2 NCEER method

Because the liquefaction phenomenon itself can not be simulated by the PLAXIS HSsmall model, a liquefaction assessment was performed with the NCEER method and the results are shown in figures 7.18 to 7.23. Comparing the compacted and uncompacted model showed that compaction increased the minimum factor of safety against liquefaction in each and every case. Depending on the spacing distance and magnitude, however, this increase was sometimes negligible.

For a magnitude 6.5 earthquake and 4 m spacing, the minimum factor of safety increased from 0.9 to 1 (figure 7.18), which a) is a very small increment, and b) 1 is still a low factor of safety. For the same magnitude but grid spacing equal to 3.11 m (figure 7.20) and 2.22 m (figure 7.22), a much higher increment was observed: 0.9 to 1.5 and 0.9 to 2, respectively. Based on this results, one could say that for a magnitude equal to 6.5 and spacing distance 3.11 m or 2.22 m liquefaction will not occur after compaction. While for a spacing of 4 m this is not the case because of the low factor of safety after compaction.

For a magnitude 7.5 earthquake the liquefaction problem was not solved by compaction according to the NCEER method. One could observe an increase in the factor of safety due to compaction, which was higher for smaller grid spacings. But the factor of safety remained below 1 in every case. Figures 7.19, 7.21 and 7.23 show the magnitude 7.5 simulations.

Comparing compacted to average model results, one could observe very similar minimum factors of safety for the models with a grid spacing of 4 m and 3.11 m and for earthquake magnitudes 6.5 and 7.5. While for the model with grid spacing 2.22 m, the factor of safety was overestimated for both earthquake magnitudes by the average model. Based on this one could say that approximating the heterogeneous compacted soil by the 'average' soil is good practice in case the grid spacing is not too small.

### 8.3 PLAXIS versus NCEER

When comparing the conclusions made in sections 8.1.2 and 8.2, the following could be observed:

- The clearly contractant behaviour which was shown by PLAXIS and indicated liquefaction, was confirmed by the NCEER method which indeed showed a factor of safety against liquefaction lower than 1 indicating liquefaction as well.
- The comparison of uncompacted and compacted models agreed reasonably well with what is simulated in PLAXIS and what was calculated according to the NCEER method. Two exceptions could be seen: 1) for spacing 4 m and magnitude 7.5 PLAXIS indicated that liquefaction could not occur (dilatant behaviour, figures 7.12c and 7.12f) while according to the NCEER method liquefaction would occur, and 2) for spacing 2.22 m and magnitude 7.5 PLAXIS indicated that liquefaction could not occur (dilatant behaviour, figures 7.16e and 7.16f) while according to the NCEER method liquefaction would occur. It was believed that these exceptions were caused by the fact that (local) liquefaction was initiated in the model and that because of this its behaviour was no longer correct since PLAXIS can not deal with liquefaction (failure).
- When comparing the results of the compacted and the average models, PLAXIS and the NCEER method showed somewhat contradictory results. While the PLAXIS results showed that the average model is a good approximation for the two smaller spacing distances and small earthquake magnitude, the NCEER method showed that the average model is only a good approximation for the two larger spacing distances and for both earthquake magnitudes. This might also have to do with the fact that liquefaction occurred in the PLAXIS model. For the largest spacing distance or for the stronger earthquake, liquefaction was likely to occur according to the NCEER method. This can explain why PLAXIS did not give reliable results in those two cases. The NCEER method is believed to be more reliable because it was developed from empirical evaluations of field measurements and field and laboratory test results. Above that it has also passed the test of time being published over 30 years ago by Seed et al. [44] and still being used. However, the method was only verified for horizontally layered soil. [43] Therefore the application to a soil containing vertical compacted 'columns' might have caused inaccuracies as well.

## 9 General conclusion

Based on the findings above, the author believes that the current practice of evaluating liquefaction resistance based on the ‘worst’ CPT result is too conservative. However, because of the contradictory results mentioned in the last bullet in section 8.3, further research is recommended to decide whether or not averaging the ‘best’ and the worst CPT result is good practice.

Because the vibroflotation process itself was not simulated and a heterogeneous compacted state of the soil was assumed at the beginning, the methods used in this thesis might also be applicable to other deep vibratory compaction methods that result in similar heterogeneous compaction grids.

## 10 Recommended research

Further research might include the use of a numerical model which is able to simulate the liquefaction phenomenon itself. This would take away the doubt whether liquefaction occurs or not which arises when using the volumetric strains from PLAXIS. Also the use of real in-situ and lab measurements can be included in the continuation of this thesis to decrease the uncertainty due to the use of multiple correlations by which the soil parameters were obtained. The use of a 3D-model is recommended to determine the effects of using a triangular compaction grid instead of a square compaction grid since this can not be taken into account by a 2D plain-strain model.

## Appendices

### A Determination of the dominant frequency in the earthquake input motion

The dominant frequency in the earthquake input motion, more exactly the input accelerations, was determined by means of the Fourier transform of the input time series. This was obtained with the commercial software Matlab using the following code:

```
Mwlow = xlsread('Earthquake_Data.xlsx', 'Time_series_Mw=6,5', 'E3:G7983');
```

```
T = 39.9;
Fs = 200;
f1=0:1/T:Fs;
t = 0:1/Fs:T;
N = length(t);
X = fft(Mwlow(:,2));
S = 2/N;
fdlow = S.*abs(X);
[M1, I1] = max(fdlow);
f1low = f1(I1)
```

```
Mwhigh = xlsread('Earthquake_Data.xlsx', 'Time_series_Mw=7,5', 'M3:O19003');
```

```
T = 95;
f2=0:1/T:Fs;
t = 0:1/Fs:T;
N = length(t);
X = fft(Mwhigh(:,2));
S = 2/N;
fdhigh = S.*abs(X);
[M2, I2] = max(fdhigh);
f1high = f2(I2)
```

The code first determined the Fourier transform. Then the maximum amplitude of the Fourier transform was determined and the corresponding frequency was returned by the code. The first part of the code did this for the magnitude 6.5 earthquake and the second part did this for the magnitude 7.5 earthquake.

## Acknowledgements

The subject of this master's thesis was provided by dredging and offshore construction company DEME n.v. with the help of Patrick Mengé, Sr. Geotechnical Engineer and Head of Geotechnics Division RMPE, and Geert Vanneste, Dredging Training and Support and lecturing professor at KULeuven. The author also appreciates the help and recommendations of Stefan Larsson, Professor in Geotechnology and Head of the Division Soil- and Rock Mechanics at KTH, Carl Wersäll, Post-Doctoral Researcher at the Division Soil- and Rock Mechanics at KTH, and Rainer Massarsch, Geo Risk & Vibration Scandinavia AB.

## References

- [1] Tsubokawa I., Ogawa Y., Hayashi T., 1964, *Crustal Movements before and after the Niigata Earthquake*, Journal of the Geodetic Society of Japan, volume 10, No. 3-4, p.165-171, The Geodetic Society of Japan
- [2] Berg G.V., Stratta J.L., 1964, *Anchorage and the Alaske earthquake of March 27, 1964*, American Iron and Steel Institute
- [3] Acacio A.A., Kobayashi Y., Towhata I., Bautista R.T., Ishihara K., December 2001, *Subsidence of Building Foundation Resting upon Liquefied Subsoil: Case Studies and Assessment*, Soils and Foundations, volume 41, No. 6, p.111-128, Japanese Geotechnical Society
- [4] Kramer S.L., 1996, *Geotechnical earthquake engineering*, Prentice-Hall Inc., ISBN: 0-13-374943-6
- [5] Ishibashi I., Sherif M.A., Tsuchiya C., June 1977, *Pore-Pressure Rise Mechanism and Soil Liquefaction*, Soils and Foundations, volume 17, No. 2, Japanese Society of Soil Mechanics and Foundation Engineering
- [6] Shibata T., Yukioto H., Miyoshi M., March 1972, *Liquefaction Process of Sand During Cyclic Loading*, Soils and Foundations, volume 12, No. 1, Japanese Society of Soil Mechanics and Foundation Engineering
- [7] Das B.M., Sobhan K., 2014, *Principles of Geotechnical Engineering, Eight Edition, SI*, Cengage learning, ISBN13: 978-1-133-10867-2, p.273
- [8] Towhata I., 2008, *Geotechnical Earthquake Engineering*, Springer-Verlag Berlin Heidelberg, ISBN: 978-3-540-35782-7, DOI: 10.1007/978-3-540-35783-4
- [9] Committee on Earthquake Engineering (Chairman: Housner G.W.), Commission on Engineering and Technical Systems, National Research Council, 1985, *Liquefaction of Soils During Earthquakes*, National Academy Press, Report No: CETS-EE-001

- 
- [10] Brown R.E., 1976, *Vibroflotation Compaction of Cohesionless Soils*, Journal of the Geotechnical Engineering Division, 1977
- [11] Massarsch K.R., Broms, B.B., 1983, *Soil compaction by VibroWing method*, 8th European conference on soil mechanics and foundation engineering, Helsinki, 23-26 May, 1983, Proceeding, Volume 1, p.275-278
- [12] Ashford S.A., Rollins K.M., Bradford V. S.C., Weaver T.J., Baez J.I., *Liquefaction Mitigation Using Stone Columns Around Deep Foundations - Full-Scale Test Results*, Transportation research record 1736, Paper No. 00-1408
- [13] Thevanayagam S., Martin G.R., Nashed R., Shenthan T., Kanagalingam T., Ecemis N., August 28, 2006, *Liquefaction Remediation in Silty Soils Using Dynamic Compaction and Stone Columns*, MCEER, U.S. Department of Transportation, Federal Highway Administration, Technical report: MCEER-06-0009
- [14] Nguyen T.V., Rayamajhi D., Boulanger R.W., Ashford S.A., Lu J., Elgamal A., Shao L., November 2013, *Design of DSM Grids for Liquefaction Remediation*, Journal of Geotechnical and Geoenvironmental Engineering, 139, p.1923-1933
- [15] Porbaha A., Zen K., Kobayashi M., March 1999, *Deep Mixing Technology for Liquefaction Mitigation*, Journal of Infrastructure Systems, 5(1), p.21-34
- [16] Seed H.B., Book J.R., July 1977, *Stabilization of Potentially Liquefiable Sand Deposits Using Gravel Drains*, Journal of the Geotechnical Engineering Division, 103(GT7), p.757-768
- [17] Kirsch K., Kirsch F., 2010, *Ground improvement by deep vibratory methods*, Spon Press, ISBN13: 978-0-415-55015-7
- [18] van 't Hoff Jan, van der Kolff Art Nooy, 2012, *Hydraulic Fill Manual (1st edition)*, CRC Press/Balkema Taylor & Francis Group
- [19] BAUER-Pileco Inc., Techniques overview, Ground Improvement, [http://www.bauerpileco.com/en/techniques/techniques\\_overview/ground\\_improvement](http://www.bauerpileco.com/en/techniques/techniques_overview/ground_improvement), 15/05/2017
- [20] Van Impe W.F., 1989, *Soil Improvement Techniques and their Evolution*, Soil Mechanical Department, Ghent State University, A.A.Balkema, ISBN:9-06-191805-7
- [21] Bo M.W., Arulrajah A., Horpibulsuk S., Leong M., Disfani M.M., 2014, *Densification of Land Reclamation Sands by Deep Vibratory Compaction Techniques*, Journal of Materials in Civil Engineering, 26(8):06014016, DOI: 10.1061/(ASCE)MT.1943-5533.0001010
- [22] Moseley M.P., Kirsch K., 2004, *Ground improvement, Second Edition*, Spon Press, Taylor & Francis Group, ISBN: 0-415-27455-9, p.82

- [23] Balachowski L., Kurek N., 2014, *Deep Compaction Control of Sandy Soils*, *Studia Geotechnica et Mechanica*, XXXVI(2), DOI: 10.2478/sgem-2014-0014
- [24] Bauduin C., 2014, *Rotsmechanica Deel 2 Bepaling van grondparameters en karakteristieke waarden*, Catholic University Leuven (H01E9a), p.64
- [25] Robertson P.K., Cabal K.L., 2015, *Guide to Cone Penetration Testing for Geotechnical Engineering (6th edition)*, Gregg Drilling and Testing Inc.
- [26] Massarsch K.R., Fellenius B.H., 2002, *Vibratory compaction of coarse-grained soils*, *Canadian Geotechnical engineering Journal*, 39(3), p.695-709
- [27] Salgado R., Boulanger R.W., Mitchell J.K., 1997, *Lateral Stress Effects on CPT Liquefaction Resistance Correlations*, *Journal of Geotechnical and Geoenvironmental Engineering*, 123(8), p.726-735
- [28] PLAXIS bv., Editors: Brinkgreve R.B.J., Kumarswamy S., Swolfs W.M., 2016, *PLAXIS Reference Manual*
- [29] PLAXIS bv., Editors: Brinkgreve R.B.J., Kumarswamy S., Swolfs W.M., 2016, *PLAXIS Material Models Manual*
- [30] Liyanapathirana D.S., Poulos H.G., 2002, *A numerical model for dynamic soil liquefaction analysis*, *Soil Dynamics and Earthquake Engineering*, 22, p.1007-1015
- [31] Liyanapathirana D.S., Poulos H.G., 2002, *Numerical simulation of soil liquefaction due to earthquake loading*, *Soil Dynamics and Earthquake Engineering*, 22, p.511-523
- [32] Brinkgreve R.B.J., Engin E., 2010, *Validation of empirical formulas to derive model parameters for sands*, In Benz T., Nordal S. (eds), *7th European Conference Numerical Methods in Geotechnical Engineering*, Numge 2010, Trondheim, volume 1, p.137-174
- [33] Youd T.L., 1973, *Factors Controlling Maximum and Minimum Densities of Sands*, *Evaluation of Relative Density and Its Role in Geotechnical Projects Involving Cohesionless soils*, ASTM STP 523, American Society for Testing and Materials, p.98-112
- [34] Heinz J. Priebe (Keller Grundbau GmbH), 1998, *Vibro Replacement to Prevent Earthquake Induced Liquefaction*, *Proceedings of the Geotechnique-Colloquium*, Darmstadt, Germany, March 19th, 1998, Technical paper 12-57E
- [35] Hashhash Y.M.A., Park D., 2002, *Viscous damping formulation and high frequency motion propagation in non-linear site response analysis*, *Soil Dynamics and Earthquake Engineering*, 22(2002), p.611-624
- [36] Brinkgreve R.B.J., Kappert M.H., Bonnier P.G., 2007, *Hysteretic damping in a small-strain stiffness model*, *Numerical Models in Geomechanics*, Taylor & Francis group, ISBN: 978-0-415-44027-1

- [37] Chopra A.K., 2013, *Dynamics of Structures, Theory and Applications to Earthquake Engineering, Global Edition, Fourth Edition*, Pearson Education, ISBN13: 978-0-13-285803-8, p.455-457
- [38] Hudson M., Idriss I.M., Beikae M., 1994, rev. 2003, *USER'S Manual for QUAD4M, a computer program to evaluate the seismic response of soil structures using finite element procedures and incorporating a compliant base*, Center for geotechnical Modelling, Department of Civil & Environmental Engineering, University of California
- [39] Wichtmann T., Triantafyllidis T., 2009, *Influence of the Grain-Size Distribution Curve of Quartz Sand on the Small Strain Shear Modulus  $G_{max}$* , Journal of geotechnical and geoenvironmental engineering, 135(10), p.1404-1418
- [40] Benz T., Schwab R., Vermeer P., 2009, *Small-strain stiffness in geotechnical analysis*, Bautechnik Special issue 2009 - Geotechnical Engineering
- [41] Pacific Earthquake Engineering Research Center, <http://ngawest2.berkeley.edu/site>, University of California, Berkeley, 13/03/2017
- [42] Zienkiewicz O.C., Bicanic N., Shen F.Q., 1989, *Earthquake Input Definition and Transmitting Boundary Conditions*, Chapter 3 in *Advances in Computational Nonlinear Mechanics*, Editor: Doltsinis I.St., Springer-Verlag Wien, ISBN: 978-3-211-82113-8, DOI: 10.1007/978-3-7091-2828-2
- [43] Youd T.L., Idriss I.M., 2001, *Liquefaction resistance of soils: summary report from the 1996 NCEER and 1998 NCEER/NSF workshops on evaluation of liquefaction resistance of soils*, Journal of Geotechnical and Geoenvironmental engineering, 127(4), p.297-313
- [44] Seed H.B., Idriss I.M., 1971, *Simplified procedure for evaluation soil liquefaction potential*, Journal of Soil Mechanics & Foundations Div., 97(9), p.1249-1273